8

Investigating Strain in Silicon-on-Insulator Nanostructures by Coherent X-ray Diffraction

Gang Xiong[1]*, Oussama Moutanabbir*[2]*, Manfred Reiche*[3]*, Ross Harder*[4]*, and Ian Robinson*[1,5]

[1] *University College London, London Centre for Nanotechnology, London WC1H 0AH, UK*
[2] *Ecole Polytechnique de Montreal, Department of Engineering Physics, Montreal, QC H3C 3A7, Canada*
[3] *Max Planck Institute of Microstructure Physics, Weinberg 2, 06120 Halle (Saale), Germany*
[4] *Advanced Photon Source, Argonne National Laboratory, Argonne, IL 60439, USA*
[5] *Condensed Matter Physics and Materials Science Department, Brookhaven National Laboratory, Upton, NY 11973, USA*

8.1 Introduction

Coherent X-ray Diffraction Imaging (CDI) has emerged in the last decade as a promising high-resolution lens-less imaging approach for the characterizations of various samples. It has made significant technical progress through developments in source, algorithm, and imaging methodologies thus enabling important scientific breakthroughs in a broad range of disciplines. In this chapter, we will introduce the principles of forward scattering CDI and Bragg geometry CDI (BCDI), with an emphasis on the latter. BCDI exploits the ultrahigh sensitivity of the diffraction pattern to the distortions of crystalline lattice. Its ability of imaging strain on the nanometer scale in three dimensions is highly novel. We will present the latest progress on the application of BCDI in investigating the strain relaxation behavior in nanoscale patterned strained-silicon-on-insulator (sSOI) materials, aiming to understand and thereby engineer strain for the design and implementation of new generation semiconductor devices.

8.2 Coherence

Coherence is the property of light and is responsible for interference effects. Spatial coherence describes the correlation between waves at different points in space, while temporal coherence describes the correlation or predictable relationship between waves observed at different moments in time, or along the direction of a beam. For classical light sources, such as a lamp, a star or synchrotron X-rays, photons are spontaneously emitted in a chaotic way, both spatially and temporally. Spatial coherence can be obtained by applying spatial filters, such as slits or pinhole, while temporal coherence can be achieved by

Synchrotron Radiation in Materials Science: Light Sources, Techniques, and Applications, First Edition.
Edited by Chunhai Fan and Zhentang Zhao.

extracting a small wavelength band using a bandpass frequency filter such as a monochromator. A direct consequence of applying these filters to obtain high degree of coherence is the massive loss of intensity; however, with the high-brilliance X-ray sources available in the third generation synchrotron sources, the cost in intensity is now affordable and therefore, coherent or partially coherent beams with low divergence can be applied to a wide range of samples. The small divergence also allows most theoretical treatments to adopt the paraxial approximation and the use of the scalar formulation of diffraction theory, neglecting polarization effects in the scattering. Here, some basic concepts related to the coherence properties of a third generation synchrotron source will be introduced to motivate CDI techniques, and their recent developments and applications will be discussed.

8.2.1 Transverse (or Spatial) Coherence Length

This property of light is due to the source not being ideally point-like and having some lateral extension, which can lead to incoherence in the transversal direction. When looking at a cross-section of a beam of light, the length over which the phase is correlated is the transverse coherence length. For example, in the case of Young's double slit experiment, if the transverse coherence length of the entering light wave is smaller than the spacing between the two slits, the resulting pattern on a screen in the far-field will no longer be a set of interference fringes with fully developed maxima and zero intensity in the minima as would be when the illumination beam is from a monochromatic point source [1–3]. The visibility of the interference fringes will be reduced, in the extreme case to two single-slit diffraction patterns. For a source of height w, with a distance R between the source and the observer, the beam is coherent over $d = \lambda R/w$, which is defined as the transverse coherence length.

It is worth noting that the transverse coherence length is a property of the source and the beamline optics, and does not depend on the specific diffraction set-up. Apart from Young's double slit, a single slit, a waveguide, or a fiber can all be used as a test object to elucidate and deduce the transverse coherent length and obtain the same result [4–6]. The above definition can be extended to a rectangular source with horizontal width w_h and vertical width w_v to yield the corresponding transverse coherence lengths $\xi_\mathrm{h} = \lambda R/w_\mathrm{h}$ and $\xi_\mathrm{v} = \lambda R/w_\mathrm{v}$ [7, 8]. The limit $R \rightarrow \infty$ or $\sigma \rightarrow 0$ indicates that the source is fully coherent with an infinitely large coherence length. Third generation synchrotron sources typically have a source size of $\sigma_\mathrm{v} \simeq 10$–$50\,\mu\mathrm{m}$ and $\sigma_\mathrm{h} \simeq 100$–$500\,\mu\mathrm{m}$. At an energy of 9 keV and a typical distance of 30 m from the source, the transverse coherence length are in the ranges of $\xi_\mathrm{v} \simeq 20$–$120\,\mu\mathrm{m}$ and $\xi_\mathrm{h} \simeq 3$–$12\,\mu\mathrm{m}$. For some beamlines that are dedicated for coherent diffraction such as the beamline I13 at Diamond Light Source, with a source-sample distance up to 220 m, the coherence lengths are larger: $\xi_\mathrm{v} \simeq 500\,\mu\mathrm{m}$ and $\xi_\mathrm{h} \simeq 30\,\mu\mathrm{m}$.

8.2.2 Longitudinal (or Temporal) Coherence Length

The temporal coherence defines the degree of coherence of the light source along its propagation direction and relates to the beam monochromaticity. The temporal coherent length is defined as the propagation distance over which two wavefronts, one with wavelength λ and the other with a slightly different wavelength

$\lambda + \Delta\lambda$, simultaneously departing from a point source are in antiphase. Therefore, $N\lambda = \left(N - \frac{1}{2}\right)(\lambda + \Delta\lambda)$, and one can deduce this distance $\xi_l = N\lambda \simeq \frac{1}{2}\frac{\lambda^2}{\Delta\lambda}$.

The longitudinal coherence length is inversely proportional to the bandwidth. For the (111) reflection of a Si crystal monochromator, $\frac{\Delta\lambda}{\lambda} = 1.3 \times 10^{-4}$. At an energy of 9 keV, the corresponding longitudinal coherence length ξ_1 is around 500 nm, much smaller than the transverse coherence length.

The longitudinal coherence length couples to the optical path length difference (OPLD) of the X-rays through the sample. When the OPLD is smaller than ξ_1 the sample is said to be within the coherent limit and meets the required conditions for coherent diffraction measurements. In the transverse directions, to achieve a full coherent diffraction the sample size should be smaller than the transverse coherence length, or a pinhole of a size smaller than the transverse coherence length can be placed just in front of the sample.

8.3 Coherent X-ray Diffraction Imaging (CDI)

8.3.1 Fundamental Concepts of Lens-Less Imaging

According to the Huygens principle, every point of an object to which a luminous disturbance reaches becomes a source of a spherical wave. The sum of these secondary waves determines the form of the wave at any subsequent time. Along the propagation direction, a short distance away from the illuminated object, the secondary waves emitted from all object points will interfere and result in scattering patterns in which the object's details are encoded. Different imaging systems can be applied to retrieve the object's details. A lens-based imaging system would typically make use of a lens to reconstruct the object image, as shown in Figure 8.1a. The lens refocuses the scattered waves with their associated phases to build the image. Lens imaging techniques can be applied to visible light, X-rays,

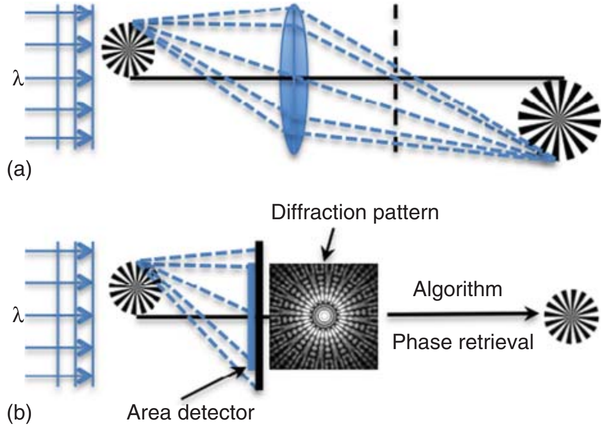

Figure 8.1 Schematic views of (a) a lens-based imaging system and (b) a lens-less imaging system where the active area of the detector is highlighted in blue. For lens-less imaging, the maximum spatial frequency collected in the diffraction pattern in principle determines the reconstruction resolution.

and electrons. In such a system, the resolution is mostly limited by lens aberrations. In comparison, Figure 8.1b shows schematically a lens-less imaging system in which the scattered beam propagates and produces a scattering pattern downstream whose intensity is then collected by a 2D detector. This recorded pattern is then used to reconstruct the object details via an iterative feedback algorithm. Effectively, the objective lens in a typical microscope imaging system is replaced with the algorithm software to convert the scattering pattern from the reciprocal space into a real space image [9].

Because the detector can only record intensities, the phase information of the scattered complex-valued waves is lost during the measurement. Applying a simple Fourier transform algorithm to the measured intensity alone is insufficient for retrieving the image, giving rise to a "phase problem." Some constraints need to be applied for both the measurement and sample image in the retrieval algorithms, and will be discussed further in subsequent sections. The advantage in using lens-less imaging techniques is that the final image is aberration-free and resolution is only fundamentally limited by the extent of the diffraction and dose. As schematically shown in Figure 8.1b, the limit is on the maximum spatial frequency collected in the diffraction pattern, which, in principle, determines the reconstruction resolution. Practically, it depends on wavelength, numerical aperture size, photon noise, and radiation damage to the sample.

If the distance between source and sample is Z_0, sample and detector is Z, the defocusing distance Z_d and the magnification factor M are then defined as $Z_\mathrm{d} = \frac{Z_0 Z}{Z_0+Z}$ and $M = \frac{Z_0+Z}{Z_0}$, respectively. In lens-less imaging, three different imaging regions can be exploited as a function of the Fresnel distance $D_\mathrm{f} \approx \frac{a^2}{\lambda}$ where a is the sample size and λ is the wavelength, as shown in Figure 8.2.

In the contact or near-contact regime ($Z_\mathrm{d} \ll D_\mathrm{f}$), the detector is placed directly behind the sample, the contrast arises as an edge-enhanced image and the sharp edges of the sample appear as characteristic fringes of oscillating intensity.

As the detector moves further away from the sample, interferences build up and the intensity distribution starts to lose resemblance with the original sample.

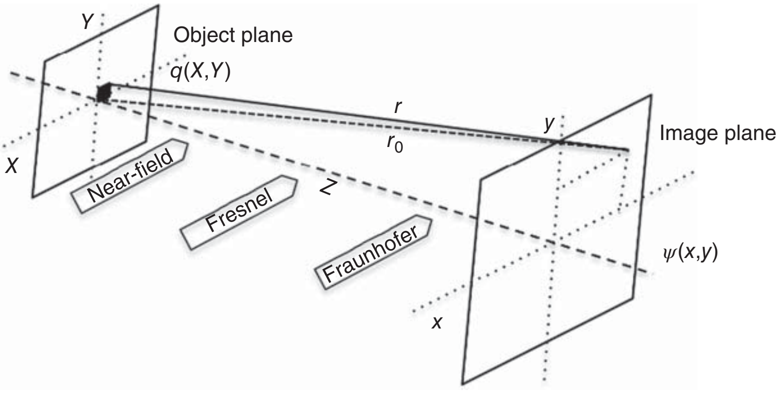

Figure 8.2 Sketch of three different imaging regions in lens-less imaging system defined as a function of the Fresnel distance $D_\mathrm{f} \approx \frac{a^2}{\lambda}$, where a is the sample size and λ is the wavelength.

The next regime to enter is the Fresnel diffraction regime ($Z_\mathrm{d} \sim D_\mathrm{f}$); it can also be called "holographic regime" as the interference pattern is formed by a large number of alternating fringes more and more closed spaced. In this regime, the diffracted amplitude can be approximated as:

$$\psi(x,y) \approx \frac{i\exp(ikr_0)}{\lambda r_0} \iint q(X,Y)\exp\left(ik\left[\frac{(-2xX-2yY)}{2r_0}\right]\right) \exp\left(ik\left[\frac{(X^2+Y^2)}{2r_0}\right]\right) dX\,dY, \tag{8.1}$$

where $q(X,Y)$ is the complex sample transmission function, with an amplitude due to absorption and a phase due to the shift of the wave propagating through the sample. The third exponential term accounts for the spherical curvature of the wavefront.

On further increasing the distance between the detector and the sample, when ($Z_\mathrm{d} \gg D_\mathrm{f}$), the curvature of the wavefront becomes negligible and the third exponential term in Eq. (8.1) becomes unity. The amplitude distribution $\psi(x,y)$ does not change shape with the distance. This defines the Fraunhofer diffraction regime. In this regime, the diffracted amplitude $\psi(x,y)$ is simply the Fourier transform of $q(X,Y)$.

8.3.2 Phase Retrieval

In a coherent diffraction imaging (CDI) measurement, as the detector can only collect the square modulus of the complex wavefields diffracted from the sample, any associated phase information is lost. To reconstruct the image of the sample from its diffraction pattern (either Fresnel or Fraunhofer regime), it is necessary to retrieve the phase information from the measured intensity. The phase retrieval algorithms used are primarily based on the iterative method of Gerchberg and Saxton, which was initially developed for the electron microscope imaging case where two corresponding sets of measurements, the magnitudes of an image and its diffraction pattern, are available [10]. With the computational tool of fast Fourier transformation (FFT) switching back and forth between the two measurement spaces, the complete wave function including both the amplitudes and phases can be determined from the intensity recorded in the two planes.

The essence of the Gerchberg–Saxton algorithm lies in the concept of oversampling in diffraction space, which implies sampling the object's density in parts of real space where it is known to be zero. The necessity of oversampling can be illustrated for one dimension case as follows [3].

In the CDI case, the detector measures only the scattered intensity $|F_0(u)|^2$, and the back-transforming results in

$$\begin{aligned} \mathcal{F}^{-1}|F_0(u)|^2 &= \mathcal{F}^{-1}[F_0(u)F_0^*(u)] = \mathcal{F}^{-1}[F_0(u)] \otimes \mathcal{F}^{-1}[F_0(u)^*] \\ &= \rho(x) \otimes \rho(-x) \equiv g(x), \end{aligned} \tag{8.2}$$

where $\rho(x)$ is the sample density distribution function and is defined as $\rho(x) = \int F(u)\exp(-2\pi iux)du$. The convolution $\rho(x) \otimes \rho(-x)$ is known as the autocorrelation function of the density. For a sample with nonzero density over a distance a, it can be seen from the definition that its autocorrelation function is nonzero over an interval w equal to twice the object size a. According to the Nyquist–Shannon sampling theorem, for a one dimensional function $g(x)$ which is nonzero within an interval w to be fully reconstructed, its Fourier transform $\mathcal{F}[g(x)]$ has to be sampled at a spacing not greater than $1/w$. Therefore, in the case here, to properly reconstruct the sample's autocorrelation function, one should measure its Fourier transform ($\mathcal{F}[g(x)] = |F_0(u)|^2$), the scattered intensity, at a spacing $1/w = 1/(2a)$. The $1/(2a)$ spacing represents an oversampling of the object's reciprocal space by a factor of 2. In the object's real space, the sampling range corresponds to a distance of twice the object size. Since one knows that the object has zero density outside its boundary, this knowledge allows the support constraint to be applied in the real space for solving the phase problem.

The above analysis for oversampling can be extended to higher dimensions. It is suggested that the oversampling by a factor of 2 refers to the corresponding multidimensional space, not to each dimension separately [11]. Typically, for a three dimensional case, the oversampling intervals along each axis can be $\Delta u_x = 1/(2^{1/3}a_x)$, $\Delta u_y = 1/(2^{1/3}a_y)$, and $\Delta u_z = 1/(2^{1/3}a_z)$, where a_x, a_y, and a_z are the sample's dimensions along the x, y, and z axes, and each of the three directions has the same oversampling ratio $2^{1/3}$.

An oversampling ratio greater than two does not provide any further information [11]. It results in a larger no-density region and renders the phasing algorithm equations overdetermined, and therefore, could yield a faster reconstruction. However, a larger oversampling ratio requires larger sample-detector distance and results in lower signal-to-noise ratio. In our experiments, we generally make sure that along each axis the oversampling ratio is not less than 3 in order to achieve rapid convergence of the reconstruction.

In the CDI case, there is only one set of measurement accomplished in the diffraction space and no corresponding measurement done in the direct space. Upgraded algorithms based on the Gerchberg–Saxton method have been developed, among which the Error Reductions (ER) and hybrid input–output (HIO) have been widely applied for phase retrieval in CDI [12–15]. The general principles and procedures of the ER and HIO are described in the following text.

As there is no measurement in direct space in CDI, one has to have some prior knowledge of the shape of the object and encode it in a compact support constraint, to aid the phase retrieval algorithm to converge [16–18]. This support constraint can be defined as half the size of the density autocorrelation function $\rho(x) \otimes \rho(-x)$. Inside the support region the electron density of the retrieved image is allowed to be nonzero and outside the support the density is padded with zeros. The phase retrieval then proceeds as shown schematically in Figure 8.3. It begins by assigning a set of random phases to the support. FFT of the support with its random phases to the reciprocal space yields a diffraction pattern that will be compared with the measured one. After replacing the calculated diffraction intensity by the measured ones, an inverse Fourier transformation (FFT^{-1}) is performed and a complex density distribution in real space can be obtained, which generally will have some nonzero values in the area outside the support. One then assigns the density to zero for the part outside the support (for the ER algorithm case) and keeps the part inside the support the same as calculated, and Fourier transforms to reciprocal space again. This iterative process is

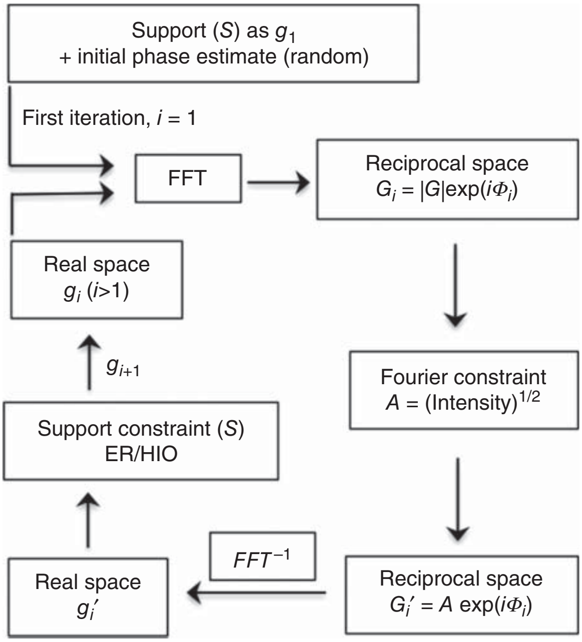

Figure 8.3 Process flow for a typical phase retrieval algorithm.

repeated until convergence is achieved, which means both the Fourier modulus constraints and the support constraint are satisfied. For a convergent solution, the error metric χ^2, defined as the difference between measured and retrieved intensity $\left(\chi^2 = \frac{\sum_i |I_{\text{calc}}(i) - I_{\text{meas}}(i)|}{\sum_i I_{\text{meas}}(i)}\right)$, typically reaches a value smaller than 10^{-3}. Here, i being the index of a given pixel in the computational array, indicates that the calculations are done on a per pixel basis.

The ER algorithm always minimizes the error between the iteration calculation and measurement, thus leaving no access to escape from the local minima of the error metric therefore often suffers from "stagnation." Typical stagnated solutions include the sum of the correct image and its centro-symmetrical inversion, lateral transformation of the object, complex conjugation, spatial inversion, and so on. The HIO algorithm has been proposed to avoid stagnation, by using a modified real space constraint [13, 19]. Instead of setting the estimated object equal to zero outside the support region, it takes into account the estimates of the previous iteration using a feedback coefficient β. ER and HIO are shown here in the following equation:

$$\text{ER}: g_{i+1}(x) = \begin{cases} g_i'(x) & (x) \in S \\ 0 & (x) \notin S \end{cases} \qquad g_i'(x) = P_M g_i(x) \tag{8.3}$$

$$\text{HIO}: g_{i+1}(x) = \begin{cases} g_i'(x) & (x) \in S \\ g_i(x) - \beta g_i'(x) & (x) \notin S \end{cases} \qquad 0 \le \beta \le 1, \tag{8.4}$$

where $g_i(x)$ is the output of the ith iteration, and $P_M = \text{FFT}^{-1} P_{|\cdot|} \text{FFT}$ is the projection operator, in which the direct and inverse Fourier transformation are represented by FFT^{-1} and FFT, respectively. The HIO algorithm has the effect of damping the regions where the amplitude should converge to zero, and provides the real space constraint that drives the algorithm toward convergence. The feedback component (the second condition in Eq. (8.4)) allows this algorithm to emerge from local minima of the invariant error metric and thus avoid stagnation. It essentially controls the convergence rate of the iterations as well. The feedback coefficient β is typically set between 0.6 and 0.9 [13, 19, 20].

It was proposed that the combination of HIO and ER outperforms both the algorithms individually, and is particularly effective in avoiding stagnation and achieving rapid convergence. The heart of this mixture of algorithms includes a number of cycles of iterations, in which one cycle typically consists of a few tens of iterations of the HIO algorithm followed by 5–10 iterations of the ER algorithm [19]. This procedure has become the workhorse of phase retrieval in coherent diffraction experiments. Recently, a guided-HIO (GHIO) approach has been applied for improving the uniqueness of a reconstructed image [21]. In GHIO, multiple sequences of phase retrieval are started from random distributions and the resulting images from each are combined together periodically during the iterations, in a variety of ways, to converge to a single solution. A number of other improved approaches have been proposed as well, including the difference map, saddle-point optimization, hybrid reflection projection, relaxed averaged alternating reflections, charge flipping, and matrix completion [22–28].

The support is also an important factor for the phase retrieval, as it will significantly influence how the electron density of the image is modified at each iteration. A loose support can result in nonunique solutions to the reconstruction [18]. Providing a tight support for the phase retrieval requires *a priori* knowledge of the object, which is not always available. With this in mind, a formulation called "shrinkwrap" has been developed, which allows for the support size to be dynamically determined as the iterations of the algorithm proceed [29]. In "shrinkwrap" reconstruction, the first support can be defined from the autocorrelation function of the object, which is readily obtained by Fourier transforming the diffraction pattern. Although both the correct object density and its centro-symmetric inversion fit within this initial support, the inversion symmetry would progressively be lost as the algorithm converges. After a certain number of iterations of the algorithm (HIO/ER), the current reconstructed object is convolved with a Gaussian of width σ to find the new support. The next round of iterations can then be launched with the new support. This process continues and the Gaussian width σ is set to reduce gradually for the support updation, to eventually achieve a stable solution.

8.3.3 Forward Coherent Diffraction Imaging

The element geometry for forward scattering CDI is fairly simple, in which an isolated object is illuminated with a highly coherent beam of X-rays and the diffraction pattern produced by the sample is measured in the far-field, as shown in Figure 8.4a. Diffraction from an isolated object is very weak in practice, so it is necessary to introduce a beam stop to prevent the direct beam from damaging

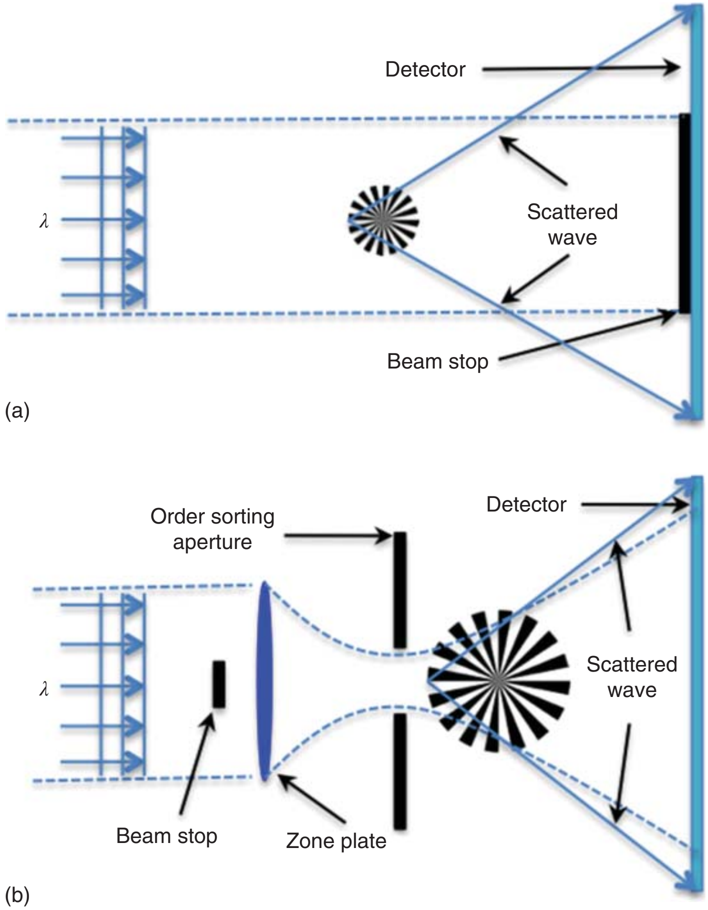

Figure 8.4 Experimental configuration for (a) plane wave forward scattering CDI, in which a coherent beam illuminates the whole sample; and (b) Fresnel CDI in which a coherent phase-curved beam generated with Fresnel zone plate illuminates either a whole sample or part of a sample.

the detector and also to facilitate the dynamic range required to properly measure the diffracted signal. The beam stop effectively prevents the measurement of the intensity at the small diffracted angles.

The first 2D image was recovered by using forward scattering CDI in 1999 [30]. A collection of gold dots, each 100 nm in diameter and 80 nm thick, was deposited on a silicon nitride membrane forming a set of letters. The diffraction patterns were taken by illuminating the sample with an incident plane wave of 1.7 nm wavelength. The reconstruction reproduced the electron microscopic image of the sample, with a resolution of 75 nm. The first 3D reconstruction of the image was achieved in 2002 with a resolution of 50 nm [31]. The reconstruction was carried out using a series of 2D diffraction patterns recorded from the noncrystalline nanostructured Ni sample. Three dimensional reconstruction was achieved by using a full range of projections later, in which the iterative process was applied directly to the 3D set of diffraction data and full tomographic images were obtained [32]. To increase the coherent flux, refractive lens and Kirkpatrik–Baez (KB) mirror systems can be used to illuminate radiation-hard samples, and higher spatial resolution can be achieved [33, 34].

Forward scattering CDI can be applied to image functional material samples [35, 36]. A typical example shows the first experimental high-resolution view inside a ceramic nanofoam, which reveals a structure consisting of nodes connected by thin beams [35]. This internal structure can be used for explaining the mechanical properties of the nanofoam and is shown to be consistent with a diffusion-limited cluster aggregation model.

Forward scattering CDI can also be realized by placing a suitable optical element (either Fresnel zone plates or waveguides) to focus the incident beam to a virtual point-like source at a position very close to the sample, as shown in Figure 8.4b [37–39]. This technique is referred to as Fresnel CDI, in which the very small source-sample distance results in spherical waves illuminating the sample and a magnified image is measured on the detector. This image uniquely defines the phase to within a constant and physically meaningless offset. The exit surface wave (ESW) at the sample can be represented as:

$$\psi_{\mathrm{T}} = \psi_{\mathrm{i}} + \psi_{\mathrm{S}}, \tag{8.5}$$

where ψ_{i} and ψ_{S} are the illumination through beam and the scattered beam, respectively. As the wave at the detector is related to the ESW at the sample by free space propagation, at the detector plane $\hat{\psi}_{\mathrm{T}} = \hat{\psi}_{\mathrm{i}} + \hat{\psi}_{\mathrm{S}}$ are simply the Fourier transform of the corresponding items in Eq. (8.5). The intensity measured at the detector can be represented as:

$$I = |\hat{\psi}_{\mathrm{T}}|^2 = |\hat{\psi}_{\mathrm{i}} + \hat{\psi}_{\mathrm{S}}|^2 = |\hat{\psi}_{\mathrm{i}}|^2 + |\hat{\psi}_{\mathrm{s}}|^2 + 2|\hat{\psi}_{\mathrm{i}}||\hat{\psi}_{\mathrm{S}}| \cos\phi. \tag{8.6}$$

As the wavefield illuminating the sample ($\hat{\psi}_{\mathrm{i}}$) is defined and known, one can see from Eq. (8.6) that the phase of the wave exiting the sample can be retrieved from the measured intensity. Fourier-transformation-based iterative algorithms have been developed for phase retrieval in Fresnel CDI [40–42]. It was further demonstrated that a finite, diverging incident beam can be used to define the boundary of an extended sample, giving rise to a finite wave exiting the sample [43]. Therefore, any part of an extended sample can be imaged, removing the limitation of the sample being finite in extent.

Although Fresnel CDI unavoidably introduces some experimental complexities as a consequence of producing the incident curved wave, there are some important benefits in using it. The presence of a low-resolution image of the object scattering function and the ability to characterize the incident beam from an independent measurement help facilitating the phase retrieval process and result in a faster convergence. Comparing with plane wave illumination, where using a beam stop for the detector is necessary and can result in a loss of low spatial frequency information, Fresnel CDI provides the possibility to measure easily the diffracted intensity at low-q. Using this method, buried structures in a semiconductor integrated circuit have been imaged [44]. Works are underway to develop 3D tomography based on Fresnel CDI [45, 46].

Another interesting development is to carry out the CDI measurement with shifting illumination, which is termed as ptychography. Traditional forward scattering CDI has some limitations, including the restriction of samples being finite size and the difficulty of convergence of the phasing algorithm. Apart from Fresnel CDI, ptychography is another technique that can be used to address these limitations. The idea of ptychography was originally proposed in the field of electron microscopy [47]. In a ptychography experiment, the sample is moved so that the beam illuminates different parts of the sample at each step, but with significant overlapping (60–90%) between illumination steps. The Ptychographical Iterative Engine (PIE) algorithm has been developed, which utilizes both the redundant information from the overlapping illumination areas on the sample and the iterative phase retrieval algorithms for the CDI, to reconstruct density distribution without the requirement of the sample being confined to a finite size smaller than the beam [48, 49]. The convergence problem associated with stagnation in local minima and nonuniqueness of the solution are overcome as well. Another advantage of ptychography is that it can be used as a tool for wavefront characterization of the focused beam due to the redundant amount of data collected [50, 51]. Simultaneously retrieval of the beam and the sample complex density function results in better reconstruction. Ptychography is a powerful tool for imaging extended samples that cannot be isolated, for example, biological tissues [52].

8.3.4 Bragg Coherent Diffraction Imaging

BCDI has recently been developed as a tool for studying nanocrystals, and has become a productive application of CDI [53–56]. By utilizing the exquisite sensitivity of the X-rays to the distortions of crystalline lattice, BCDI's ability of imaging strain on the nanometer scale in three dimensions is highly novel. BCDI recovers the complex electron density of the samples with picometer sensitivity and is sensitive to lattice distortion within nanocrystals. The "picometer sensitivity" refers to strain sensitivity much finer than the atomic spacing. The spatial resolution of the retrieved image itself is around 20 nm in these experiments. The ability to achieve picometer sensitivity from a lower resolution measurement is attributed to the fact that the strain fields are long-ranged, therefore atomic level defects, such as dislocation loops, can be identified by their strain signatures. In this section, we will introduce the fundamental principles and typical experiment set-up of BCDI, as well as the recent progress on its development.

The diffraction pattern of an infinite crystal is the product of the reciprocal lattice and the molecular transform. For a finite crystal, however, the difference is that the diffracted pattern is convolved with the Fourier transform of the crystal shape. The diffraction pattern is the standard crystalline diffraction pattern with a distribution of the intensity at the location of the Bragg diffraction spot. Figure 8.5a shows a 2D crystal with hexagonal shape on the left (where the dots correspond to lattice points) and its simulated diffraction pattern in reciprocal space on the right. As explained earlier, the finite size of the crystal results in the extension of the intensity distribution at the Bragg peaks. Furthermore, as an ideal

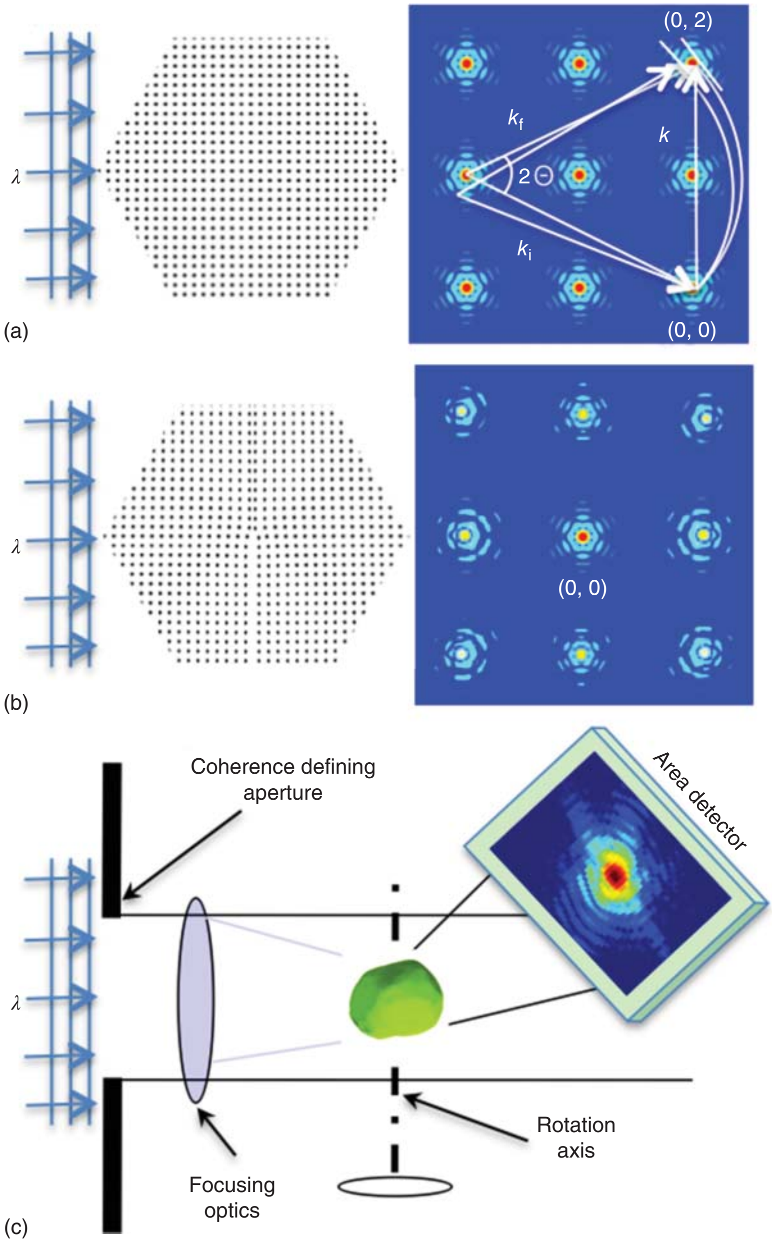

Figure 8.5 (a) Schematic view of a hexagonal-shaped crystal, where the dots correspond to lattice points (left); and the corresponding diffraction pattern in reciprocal space (right). Also shown here are the incoming ($\boldsymbol{k}_i$) and outgoing ($\boldsymbol{k}_f$) wave-vectors sketched according to the Ewald construction. As the crystal is rotated the diffraction patterns are collected by the detector (shown as a straight line perpendicular to the $\boldsymbol{k}_f$ direction). (b) A crystal with the same size and shape as the one in (a), but with an edge dislocation inside the crystal (left) and the corresponding diffraction pattern in reciprocal space (right). (c) Typical experimental setup for Bragg CDI.

finite crystal with a zero displacement field, the extended intensity distributions are locally centro-symmetric.

Any nonzero displacement field of the atoms in the crystal from their ideal lattice positions (strained crystal), however, will lead to asymmetric intensity distribution at the Bragg spots. Figure 8.5b shows, on the right, the simulated diffraction pattern for the same crystal as in Figure 8.5a but with an edge dislocation formed by inserting an extra layer of atoms in the top half of the crystal (Figure 8.5b on the left). The diffraction intensity distributions around the Bragg spots are no longer symmetrical due to the nonzero displacement field inside the crystal caused by the edge dislocation defect. Except the distribution around the (0, 0) Bragg peak, it is only sensitive to the shape of the crystal and remains unchanged.

To describe the scattering from a strained crystal, the displacement field of the atoms from their ideal positions can be represented as:

$$u(r) = r - r_0, \tag{8.7}$$

where r is the position of the atom in the crystal and r_0 the ideal position of atom in the crystal, respectively.

For coherent and monochromatic scattering, within the kinematical approximation the scattering amplitude is given by

$$A(\boldsymbol{k}) = \int d\boldsymbol{r} g(\boldsymbol{r}) e^{-i\boldsymbol{k}\cdot\boldsymbol{r}} = \mathrm{FFT}(g(\boldsymbol{r})), \tag{8.8}$$

where $\boldsymbol{k} = \boldsymbol{k}_\mathrm{f} - \boldsymbol{k}_\mathrm{i}$ is the scattering vector ($\boldsymbol{k}_\mathrm{i}$ incoming and $\boldsymbol{k}_\mathrm{f}$ outgoing wave-vectors, $|\boldsymbol{k}_\mathrm{i}| = |\boldsymbol{k}_\mathrm{f}| = 2\pi/\lambda$, λ is the wavelength), $g(\boldsymbol{r})$ is the complex-valued electron density of the crystal and is given by

$$g(\boldsymbol{r}) = \rho(\boldsymbol{r}) e^{i\boldsymbol{k}\cdot\boldsymbol{u}(\boldsymbol{r})} = \rho(\boldsymbol{r}) e^{i\boldsymbol{\phi}(\boldsymbol{r})}, \tag{8.9}$$

where $\rho(\boldsymbol{r})$ is the 3D scattering factor distribution within the crystal, $\boldsymbol{\phi}(\boldsymbol{r}) = \boldsymbol{k}\cdot\boldsymbol{u}(\boldsymbol{r})$ is the phase factor.

The experimentally measured intensity $I(\boldsymbol{k})$ is related to the scattering amplitude $A(\boldsymbol{k})$ by [57]

$$I(\boldsymbol{k}) = A^*(\boldsymbol{k}) A(\boldsymbol{k}) = |\mathrm{FFT}(g(\boldsymbol{r}))|^2. \tag{8.10}$$

When the transverse coherence length of the incident beam is larger than the dimension of the crystal sample and the diffraction pattern is adequately oversampled, one can reconstruct $g(\boldsymbol{r})$, the complex-valued electron density of the crystal, from the measured intensity distribution around the Bragg spot using the phase retrieval approaches discussed in Section 8.2.2. And the reconstructed complex electron density comprises both the amplitude, corresponding to the crystal morphology, and the phase, which is related to the displacement field (a phase of 2π represents a displacement from the ideal lattice position with a distance equal to the lattice spacing in the scattering vector direction). The strain is related to the displacement field by [58]

$$\varepsilon_{ij} = \frac{1}{2}\left(\frac{\partial u_i}{\partial \boldsymbol{x}_j} + \frac{\partial u_j}{\partial \boldsymbol{x}_i}\right), \tag{8.11}$$

where x_i is the spatial coordinate in the orthogonal direction i. BCDI is therefore potentially a powerful tool for investigating strain-related phenomena, including crystal defects, strain relaxations in semiconductor devices, phase transition, and so on. In this report, as will be shown in next section, BCDI's ultrahigh sensitivity to lattice strain is exploited to investigate the strain distribution in sSOI structures, aiming to understand and thereby engineer strain properties for design and implementation semiconductor devices.

In the Bragg reflection vicinity there is another advantage with respect to the forward scattering CDI: the 3D reciprocal space mapping becomes much easier [54]. A slight rotation of the crystal has the effect of rapidly rocking the diffraction spot through the diffraction condition. Figure 8.5a, on the right, illustrates the case for the measurement at the vicinity of reflection (0,2). The incoming ($\boldsymbol{k}_\mathrm{i}$) and outgoing ($\boldsymbol{k}_\mathrm{f}$) wave-vectors are sketched according to the Ewald construction. During the measurement, the sample is rotated through the Bragg condition for acquiring a sequence of nearly parallel patterns, which are shown as straight lines perpendicular to the outgoing wave-vector. This procedure is equivalent to shifting the detector perpendicular to the Ewald sphere in reciprocal space. Because the diffraction pattern that surrounds a reciprocal lattice point is located far from the origin, the entire intensity distribution spans only a small angular range, which in most cases lies within a 1° sample rotation range. By contrast, the forward scattering version of the experiment requires a complete 180° rotation. This principle can be extended to 3D reciprocal space, and by using a 2D detector to collect the diffraction slices at each rotation step and stacking them together, a full 3D diffraction pattern can be obtained.

Figure 8.5c shows a schematic representation of a typical BCDI experiment set-up. A monochromatic X-ray beam is selected by passing the beam through a Si-(111) double crystal. A set of JJ slits is used to select a coherent beam with a size of a few tens of microns, followed by focusing optics, such as a pair of Kirk–Patrick Baez mirrors or a Fresnel zone plate, to focus the beam down to a range of less than a 100 nm–2 μm. It is worth noting that the focusing optic is used for concentrating the coherent beam and maximizing the flux illuminating on the nanocrystal sample, and does not determine the resolution of the reconstructed image. The single crystal sample, positioned downstream, is then illuminated by the focused beam. Diffraction patterns are gathered by rotating the sample through the Bragg condition in small increments, typically 0.002–0.01° determined by the oversampling condition. At each step, 2D slices of the diffraction pattern are acquired by the X-ray detector and subsequently collated to form a complete 3D diffraction pattern for reconstruction.

The first successful 3D quantitative phase retrieval was demonstrated on a lead nanocrystal that was crystallized in ultrahigh vacuum from a droplet on a silica substrate [55]. A three dimensional image of the density, obtained by inversion of the coherent X-ray diffraction, shows the expected facetted morphology, but in addition the 3D displacement field mapping revealed a real space phase that is consistent with the three dimensional evolution of a deformation field arising from the superimposes of an interfacial contact force from classical point defects.

As can be seen from Eq. (8.9), the phase factor is the scalar product of the displacement field and the scattering vector, and therefore, only the component of the displacement field corresponding to its projection in the scattering vector direction can be retrieved from a single diffraction measurement. In order to obtain the full strain tensor in a crystal, it is necessary to measure at least three noncoplanar Bragg spots. This has been demonstrated in a recent work, in which a ZnO nanorod was measured at six different Bragg peaks [59]. From each diffraction pattern, a 3D map of the displacement field's component along the corresponding scattering vector direction is retrieved. By combining these components, all three Cartesian components of the displacement field in the nanorod, and in turn the full nine-component strain tensors, have been imaged for the nanorod.

Another progress is the added ability of the retrieve algorithm to correct for imperfect coherence in the incident X-ray beam [60]. The imperfection in coherence can be due to the scatter from window that the beam passes through, or slits open to a size wider than the beam coherent length even though this would allow one to utilize more flux to reduce the measurement time. Partially coherent wavefield illumination can reduce the contrast between the bright and dark regions of the diffraction pattern. In real space, the recovered density amplitude will typically have unphysical density modulations and be less uniform [53, 61, 62]. Therefore, it is ideal to perform CDI measurement with a fully coherent beam. However, many CDI experiments use third generation synchrotron or electron sources that can be far from fully coherent [42, 63–65]. Efforts have been made in adapting the current algorithms to accommodate both spatial and temporal partial coherence [66–69]. In recent developments, modal methods have been introduced, which assume that the recorded diffraction is made up of a number of independent modes, with the recorded diffraction being the incoherent sum of each mode's intensity. With this modified modulus constraint, 3D *ab initio* phasing of partially coherent diffraction patterns has been demonstrated. Image quality can be improved while simultaneously recovering the coherence properties of the illuminating wavefield without *a priori* assumptions [60].

One of the significances of nanoscience is the emergence of new phases of matter with novel functions at small sizes and size-dependent phase transitions. In BCDI, these behaviors will be detectable as displacement field (phase) variations within the nanocrystals. Strong surface segregation effects during the intermixing of alloy formation can be observed as the complex density changes, as in the case for surface vacancy diffusion. With the ability to achieve quantitative 3D imaging of lattice strain on the nanometer scale, BCDI is becoming a powerful technique for the structural characterization of nanomaterials and devices. A wide range of applications have been exploited based on the BCDI technique, typical examples including the studying of nanocrystals [70–75], nanowires [76–81], catalyst microcrystals [82, 83], materials under high pressure [84], lattice dynamics [85, 86], and examination of the diffusion behaviors inside nanocrystals [87], among others [88–97], by analyzing the structure, defect, and strain either in the static or the dynamic process. In the following section, we will focus on the progress on the strain distribution investigation in sSOI structures, in which the strain plays a critical role in enhancing device performance.

8.4 Strain Distribution in Silicon-on-Insulator (SOI) Structures

8.4.1 Silicon on Insulator

In the semiconductor industry, Moore's law predicts that the number of transistors per square inch, and the chip performance will be doubled approximately every 18 months [98]. This law has proven to be amazingly accurate since 1960, in part because it has been used to guide long-term planning and to set targets for research and development. The exponential scaling trend in the reduction of the feature size in integrated circuits has enabled the microelectronic industry to produce products with impressive increase in computational capability. This relentless progress toward miniaturization has led to a continuous shrinkage in the channel width from a few micrometers in the early 1970s to below 10 nm in the current and planned technology nodes [99]. However, it has indeed taken countless great efforts from engineers and scientists to avoid the realization of many predictions of a near-term end of device scaling in the past. This scaling trend is expected to hit the fundamental limits when the channel width reaches the atomic dimension. New materials or (and) device structures are thus needed to sustain the current rate of progress in device technology.

Silicon-on-insulator (SOI) structures, consisting of a film of single crystalline Si separated by a layer of SiO_2 (or sapphire, but less often) from the bulk silicon substrate, have been proposed and developed as an alternative substrate to extend the lifetime of the traditional silicon-based metal-oxide-semiconductor field-effect-transistors (MOSFET) [100, 101]. Since around 2000, commercial applications of SOI have grown rapidly and have entered the mainstream of ultralarge scale integration (ULSI) electronic circuits.

The addition of an insulator layer below the device junction layer can greatly reduce the junction capacitance and leakage current, and brings a few striking advantages [102–105]. First, as the features in the microchip keep scaling down and approaching the end of "the international technology road map for semiconductors" [99], applying SOI technology can keep the traditional Si technology going besides creating new horizons for a variety of innovative applications. MOSFETs with gate lengths of 25 nm or less do not perform well when built on bulk Si. The electric field in the transistor channel induced by the gate has to compete with the field from the source and drain regions. When the source and drain are brought into proximity the gate can lose the control of the channel electric carriers. It cannot turn off the device and the transistor ceases to function. These short channel effects (SCEs) are reduced or eliminated by going to thin SOI structures as they eliminate most of the leakage paths. And for the same supply voltage, microprocessors run faster in SOI than in bulk Si. Alternatively, it is possible to lower the operating voltage for SOI chips while still keeping the same clock rate as in the bulk Si circuits, thus reducing the power consumption.

Devices built on SOI are radiation-hard, as the majority of charges generated by a radiation particle hitting on a Si substrate would be retarded by the buried oxide layer. Other developments using SOI include power- and high-voltage devices, and high-temperature circuits [106].

sSOI has emerged as a new variety of SOI materials with enhanced capabilities. It has the same structure sequence as SOI, but with the top layer being a strained single crystalline silicon instead [107, 108]. It combines the advantages of SOI technology and that of the strained silicon. Strained silicon is adopted in an attempt to enhance the carrier mobility, as it can improve device performance beyond any benefits from device scaling and the addition of an insulator layer below the devices as in SOI. Strain engineering alone has been proved both experimentally and theoretically to enable drive current enhancement of ~4.5 times for Si p-type metal-oxide-semiconductor field-effect-transistors (pMOSFETs) (compressive strain) and ~2 times for n-type metal-oxide-semiconductor field-effect-transistors (nMOSFETs) (tensile strain), without a significant increase in leakage current [109, 110]. Since the 65 nm technology node, strain has been introduced to improve the carrier transport in Si-based complementary metal-oxide-semiconductor (CMOS) devices.

The use of strain as technology booster relies on its effect on altering silicon band structure. Figure 8.6 shows the biaxial tensile strain (in the x–y plane) effects on the conduction and valence bands of tensile strained silicon [111]. In this case, the spacing between the atoms in the plane of the wafer is bigger than it is for regular silicon. For the bulk silicon, there are six degenerate valleys with the minimum energy located near the X point in the conduction band. The tensile strain breaks this degeneracy, and shifts and splits these sub-bands, causing the energy of the Δ_2 sub-band to shift down and the energy of the Δ_4 to shift up. These will result in electrons repopulating from the Δ_4 sub-band to the Δ_2 sub-band, as shown in Figure 8.6a. The effective mass of electron in Δ_2 valley is much smaller than that in the Δ_4 valley, and the repopulation into Δ_2 has an effect of reducing the average effective mass of the electrons thus increasing the electron mobility [112]. The phonon scattering rate also changes due to the band splitting. The band splitting causes the decrease of the density of states (DOS), and therefore,

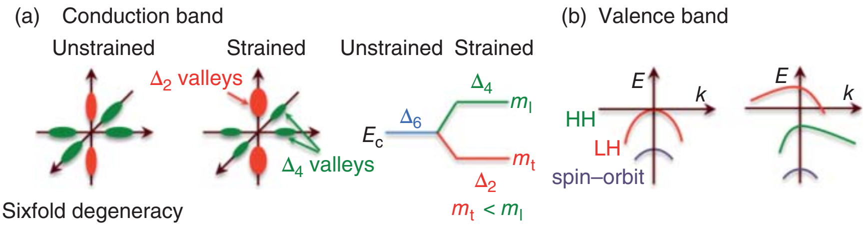

Figure 8.6 Biaxial tensile strain effects on the conduction and valence bands of silicon (100). (a) In the conduction band, the sixfold degeneracy is lifted and electrons become repopulated into the lower energy Δ_2 sub-band, which causes the average effective mass to decrease and inter-band scattering to reduce, thereby increasing the electron mobility; (b) in the valence band, the hole mobility enhancement is mainly due to the reduction of the phonon scattering caused by the lifting of the twofold degeneracy and lowering of the spin-off band.

the inter-band scattering rate becomes lower and contributes to the increase of the electron mobility [113].

In the valence band, for bulk silicon the band minimum is located at the Γ point, where the heavy-hole and light-hole bands are degenerate. As shown in Figure 8.6b, in contrast with the conduction band, the shape of the sub-bands become changed under strain and this is referred to as "band warping." The lifting of the degeneracy between light-hole and heavy-hole bands and lowering of the spin-off band, result in the reduction of inter-band and intra-band phonon scatterings, which is the main factor in the hole mobility improvement, rather than the reduction of the effective carrier mass which is the dominant mechanism in the conduction band [114].

Various methods can be used for introducing strains in semiconductor devices during fabrication. Etch-stop nitride and embedding SiGe in the source/drain region are among the most widely used approaches [115, 116]. In these cases, the strains are generated locally during transistor processing. This approach, known as a local strain process, and the strains induced are typically uniaxial. sSOI, on the other hand, is used in global strain processes, where the devices are directly built on the strained silicon. The fabrication of sSOI substrate requires technique development on both strained silicon heteroepitaxy and SOI. To obtain tensile strained silicon layer, gemanium is an ideal template substrate for the epitaxial growth, as it has the same crystal structure as silicon but with a larger crystal lattice. However, in practice, to avoid generating large numbers of crystalline defects, such as misfit and threading dislocations, SiGe alloys are used as the growth template. For example, a SiGe template layer incorporating 20% Ge will usually have a dislocation density below 10^5 cm^{-2}. The lattice mismatch can also be controlled by adjusting the ratio of Si to Ge in the template. Figure 8.7 shows schematically a typical process flow for sSOI fabrication. The first step is to epitaxially grow a SiGe buffer layer on bulk silicon, with the fraction of germanium starting from zero at the bottom and going up to the final value (e.g., 20%) at the top (Figure 8.7a). The SiGe template layer is then grown with the same lattice constant as the top of the buffer layer. This template layer has no strain in it and is therefore "relaxed," and this allows an optimally tensile strained silicon layer to grow on it subsequently (Figure 8.7b).

After the growth, hydrogen ion implantation is applied to the obtained heterostructure under ion-cut optimal conditions (Figure 8.7c) [117]. The implanted wafer is then bonded onto a handle wafer, which consists of a silicon substrate with a SiO_2 insulator layer on the top deposited by thermal oxidation or in a plasma-enhanced chemical vapor reactor (Figure 8.7d). Thermal annealing at an intermediate temperature (~500 °C) induces micro-cracking, which results in exfoliation around the implantation depth (Figure 8.7e). A strained Si thin layer on an insulator (sSOI) is obtained after the removal of the residual SiGe buffer layer using selective chemical etching (Figure 8.7f). The thickness of the strained silicon layer is usually in the range of approximately 10–30 nm. Thicker layers can be obtained by additional homo-epitaxial growth without significant relaxation of the strain. For a 0.6% initial strain it has been found that the strain can be preserved during the subsequent homo-epitaxial growth up to a thickness of 60 nm [118].

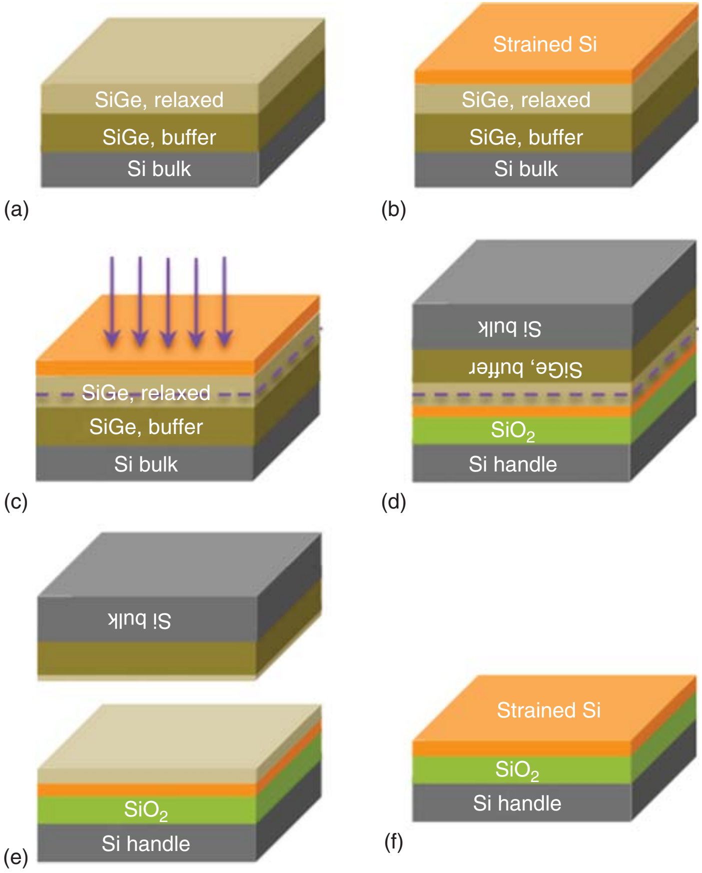

Figure 8.7 Schematic presentation of the process flow for the fabrication of an sSOI wafer. (a) Growth of the relaxed SiGe substrate; (b) growth of the biaxially tensile strained Si on the SiGe substrate; (c) hydrogen ion implantation into the grown heterostructure; (d) bonding of the hydrogen implanted heterostructure to a SiO$_2$/Si substrate; (e) thermal annealing induced layer exfoliation around the hydrogen implantation depth; (f) strained Si layer directly on SiO$_2$/Si obtained after the removal of the residual SiGe with selective etch.

8.4.2 Strain Distribution in sSOI Structures

The application of strain engineering in device fabrication raises fundamental questions about the evolution and stability of the strain during different processing steps. It was shown that the strain in sSOI can be maintained during high-temperature annealing [119]. However, the effective strain in semiconductor structures can still be drastically altered due to the integration process, particularly the active region patterning [120, 121]. There is strong motivation to understand the fundamental properties of strained Si structures during the different steps of processing, which requires accurate probe of the local strain.

Recent progress in probing the strain distribution in nanostructures includes utilizing Raman spectroscopy [122–124], transmission electron microscopy (TEM) based techniques [125–127], and X-ray diffraction based techniques, such as microbeam X-ray diffraction [128, 129], high-resolution X-ray diffraction [130, 131], and grazing incidence X-ray diffraction (GIXRD) [132]. Raman spectroscopy provides a fairly good spatial resolution and does not require any specific sample preparation, but it is limited to bare Si structures as the top metallic layer in the device prohibits the laser penetration. The heating of the sample by the laser have to be dealt with carefully in order to avoid any parasitic frequency shift, especially for thin Si layers on SiO_2, where the thermal conductivity is poor. Therefore, a careful experimental protocol is needed.

The latest TEM-based techniques, such as nanobeam diffraction and dark-field holography, enable sub-10-nm resolution in strain mapping [127]. Nevertheless, the major limitation of these techniques has to do with the relaxation during TEM specimen preparation, which not only requires mechanical simulations for interpreting the data but also results in uncertainties in strain analysis. High-resolution X-ray diffraction and GIXRD allow characterizing the strain without special sample preparation. However, as the beam footprint on the sample is in the millimeter scale, those techniques integrate and average the reflection intensities of a number of structures. Very small deviations from ideal periodicity can cause the smearing out of any ultrafine fringes [131].

BCDI with the nature of extreme sensitivity to lattice distortion (strain), high spatial resolution, and the possibility of measuring embedded devices during “operando”, has clear advantages compared with the aforementioned techniques in characterizing strain distribution in micro- and nanostructured semiconductor devices. BCDI-based ptychography has been applied to probe the strain distribution in a semiconductor device prototype [133, 134]. A probe beam was focused down to 85 nm and scanned over an epitaxial stressor layer of a SiGe-on-SOI structure with a step size of 25 nm, and 2D slices of diffraction around the (004) SiGe Bragg peak were collected at each step. The reconstruction reveals that the internal strain profile consisted of two competing lattice distortions, one from the rotation of the SOI lattice and the other from the SiGe near-edge film mismatch response. The sum of the two distortions quantitatively accounts for the asymmetric SiGe lattice slope profile observed in the Bragg ptychography measurements [134].

Here we present the progress on applying BCDI to study the strain relaxation behaviors due to lithography patterning for individual and multiple sSOI structures [135].

8.4.2.1 Strain Relaxation in Individual sSOI Structures

In this work, sSOI wafers consisting of ultrathin strained Si film with a thickness of 20 nm were used for investigation. The strained Si film was epitaxially grown on a $Si_{0.84}Ge_{0.16}$ layer. Using direct wafer bonding and the ion-cut process as described earlier, the strained Si layer was then transferred onto a Si wafer with a 200-nm-thick SiO_2 layer in between. The transferred layer is under a biaxial tensile strain of 0.6% as measured by Raman spectroscopy. In the X-ray measurement we compared the (-111) Bragg 2θ angles between the sSOI layer before patterning and the unstrained Si, and there was a 0.05° shift between them which is in agreement with the existing 0.6% biaxial tensile strain.

Electron-beam-lithography process was applied to pattern the sSOI layer, as schematically shown in Figure 8.8. A negative resist is spin-coated on the sSOI substrate. Then, a square array (20 × 20) of square elements with a lateral dimension of 1 μm, separated by 100 μm, was patterned on the negative resist by electron beam exposure. After development, the areas exposed by the electron beam remained on the substrate and reactive ion etching (RIE) was applied to transfer the pattern to the strained layer, leading to an array of square strained Si structures on oxide. The patterned islands are aligned along the ⟨110⟩ direction.

The etching was performed at −60 °C using a mixture of SF_6 (100 sccm) and O_2 (5 sccm) with a relatively low power of 40 W. The etch condition is optimized so that the chemical reactivity is dominant and the edges are formed with minimum damages, as confirmed by high-resolution TEM investigations, shown in Figure 8.9a. Figure 8.9b displays a typical atomic force microscopy (AFM) image of the investigated structures. The square has a lateral size of $950 \times 950\ \text{nm}^2$ slightly below $1 \times 1\ \mu\text{m}^2$, indicating a small shrinkage of the transferred pattern, which could be due to fluctuations during one of the pattering steps. The cross-section profile (Figure 8.9c) of the structure shows

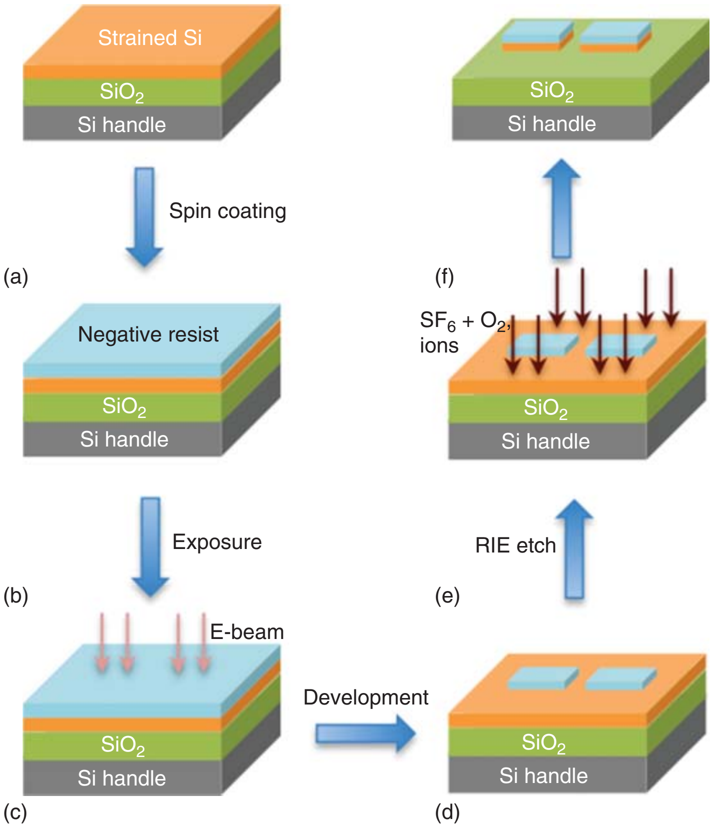

Figure 8.8 Schematic presentation of the process flow for patterning square strained silicon structures on an sSOI substrate, using E-beam lithography.

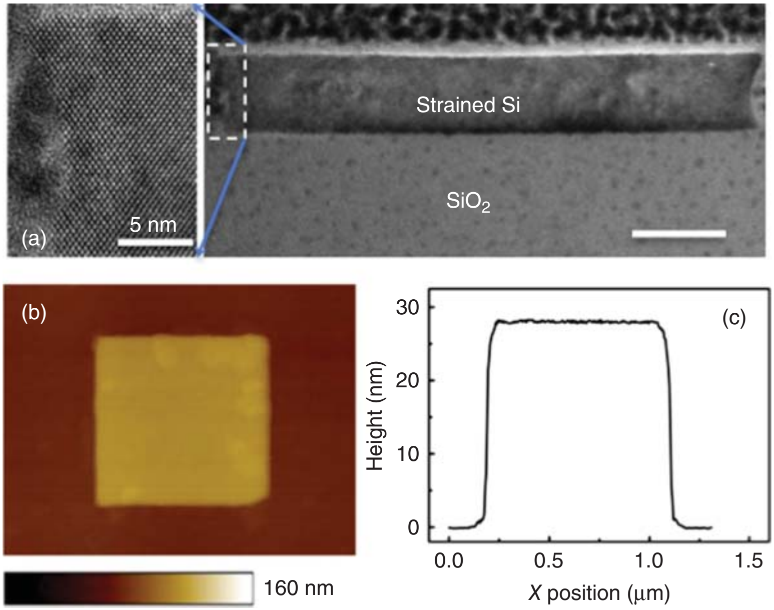

Figure 8.9 (a) High resolution TEM image of the edge profile of the strained-silicon-on-insulator structure after RIE etch; inset is the zoomed in view; (b) AFM image of a 20 nm thick 1 μm × 1 μm strained Si structure and (c) the height profile across the center of the structure.

that the island has a height of 28 nm, which means that the etching has gone deep enough to cut through the 20-nm-thick Si layer ensuring that every square is an isolated structure. As we shall see later, this over-etch also has a significant influence on the strain relaxation of the patterned structure.

The BCDI experiments were performed at the Advanced Photon Source, Argonne National Laboratory, Beamline 34-ID-C. Figure 8.10 shows the schematic drawing of the experiment geometry. A 9 keV coherent X-ray beam

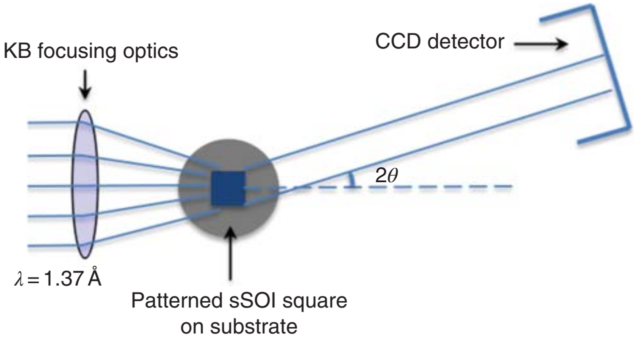

Figure 8.10 Schematic drawing of experimental geometry. The detector was positioned 1.5 m from the sample, with in-plane angle $\delta = 21.3°$, out-of-plane angle $\gamma = 14.6°$, Bragg angle $2\theta = 25.3°$ for Si (−111) diffraction.

was focused to about 1.5 μm with Kirkpatrick–Baez mirrors, so the beam size is enough to fully illuminate a single patterned square sSOI structure. Because of the large separation (100 μm) between neighboring square elements, and a higher incidence angle (8°), it is ensured that only the diffraction signals from one individual square structure is collected. Diffraction patterns were measured for by rotating the sample along the rocking curve of the (−111) Bragg reflection. A charge coupled device (CCD) detector with 20.0 μm pixel size was positioned 1.5 m downstream of the sample, with in-plane angle $\delta = 21.3$, out-of-plane angle $\gamma = 14.6°$, and total Bragg angle $2\theta = 25.3°$ to collect the 2D diffraction slice for each rotation step. The step size and detector distance are chosen so that the oversampling ratio is not smaller than 3 along any direction.

Figure 8.11a is the 2D diffraction pattern at the center position of the (−111) rocking curve, collected by the CCD detector. Figure 8.11b is the 3D diffraction pattern obtained by stacking all the collected 2D frames along the rocking curve, with the projection in the direction perpendicular to the sSOI thickness axis. They both present an asymmetrical distribution of the diffraction fringes, which is the characteristic of the investigated structure being strained.

The 3D pattern was inverted using a HIO phase retrieval algorithm with a cuboid-shaped support and a $[-\pi/2, \pi/2]$ phase constraint. Figure 8.12a,b illustrate the reconstructed magnitude and phase of the square structure. Here, a phase of 2π represents a displacement from the ideal lattice position with a distance equal to the lattice parameter in the {−111} direction, which is 0.3134 nm. The magnitude shows that the structure has a lateral size of 930–940 nm, consistent with the AFM measurement. The phase map shown in Figure 8.12b represents the displacement along the Q-vector direction, which is aligned along the horizontal edges of the square for the (−111) reflection, pointing to the left as shown by the arrow. It can be seen that there are two strong phase stripes near the left and right edges, and the corresponding displacements are relatively compressive and point to the center. The fact that the edges are contracted is attributed to the formation of free surfaces from the RIE patterning, which leads

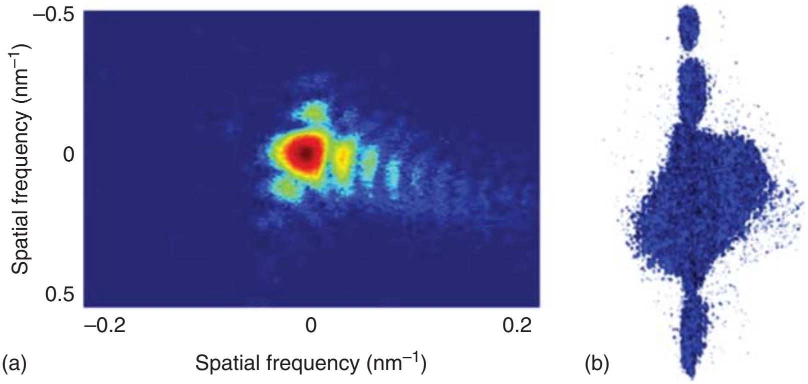

Figure 8.11 (a) The 2D diffraction frame collected at the center position of the rocking curve; (b) the 3D diffraction pattern obtained by stacking the collected 2D frames together, projected in the direction perpendicular to the sSOI thickness axis.

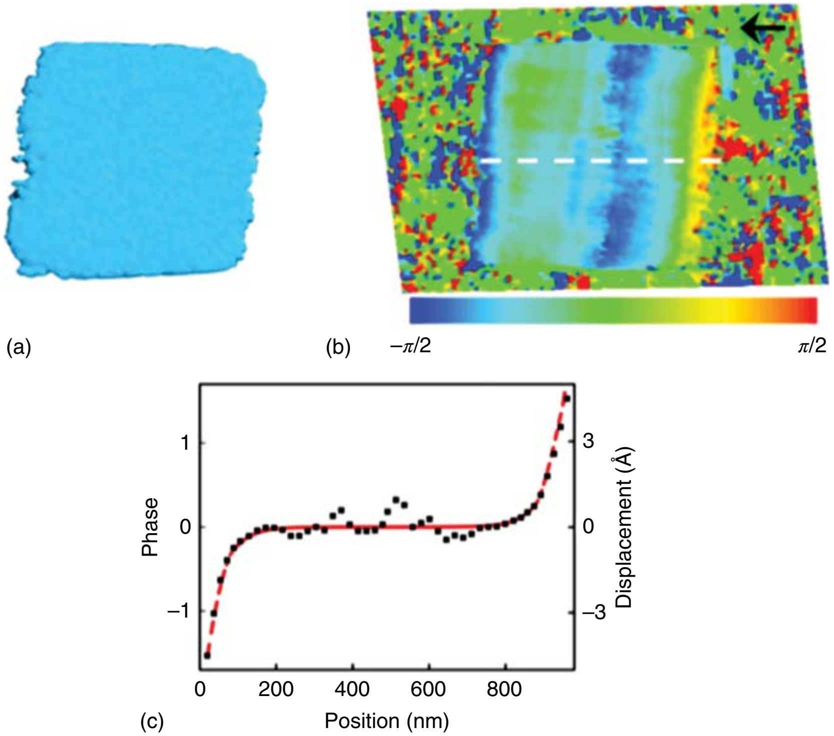

Figure 8.12 The reconstructed amplitude (a), phase (b), and a cross-section plot of the phase variation along the *x* direction (black square), with the COMSOL-simulated displacement (red dashed line) (c).

to relaxation of the initial tensile strain in the film. The relaxation is pronounced in the region within ~150 nm from the edges and rapidly attenuates toward the center where the initial strain is preserved.

It is worth pointing out that the contraction is observed on the vertical edges. As discussed in Section 8.3.1, the displacement component vertical to the scattering vector cannot be detected. In the geometry of this experiment, the scattering vector for the (−111) reflection is mostly parallel to the horizontal edges of the sSOI square as shown in Figure 8.12b, and is, therefore, less sensitive to the vertical component of the contraction.

According to Rayleigh wave solution of the continuum elasticity equation, the strain surrounding a surface distortion should die off exponentially inside the solid with a decay length similar to the disturbance size. To examine the strain decay behavior, the phase shown along the dotted line in Figure 8.12b was extracted and the result is shown in Figure 8.12c. It is found that the phase change does follow an exponential decay, and by fitting the experimental data, the decay length can be derived, which is 50 ± 15 nm. Some other models can also be used to explain this strain relaxation behavior. For example, the “shear-lag” approximation and the “lap shear” model predict a hyperbolic cosine dependence on stress with respect to distance, which will also display an exponential decay near the edges [128]. However, the distributed force model underestimates the elastic relaxation due to the free edges and does not show good agreement with the experiment results here [136]. BCDI has the potential of being applied as a tool for distinguishing between the different models of strain relaxation with nanoscale accuracy. Figure 8.12b,c also show that there are some positions in the film where the phases deviate from the base line; this may be due to the presence of dislocations or misfit defects in the film during the epitaxial growth of strained Si on SiGe.

3D finite element analysis (FEA) was carried out using the COMSOL Multiphysics software, to gain more insight into the relaxation phenomenon. Figure 8.13a is the schematic side view of the modeled system. It consists of a 20 nm thick $L \times L$ Si square on top of a 1 μm thick SiO_2 layer and an additional thickness, d, of SiO_2 underneath the structure to account for possible over-etching from the RIE process. Both materials show linear elasticity in the calculations. An initial tensile strain of 0.6% was applied to the Si layer. The relaxation phenomenon was then simulated by taking away the constraints at the free facets and allowing the system to achieve equilibrium. Simulation results show that without over-etching ($d = 0$ nm), the model predicts a too-short relaxation decay length. Manual optimization of the model yields $L = 940 \pm 20$ nm and $d = 9 \pm 4$ nm.

Figure 8.13b shows the simulated in-plane displacement component along the x direction for $L = 940$ nm and $d = 9$ nm. It can be seen that the relaxations are pronounced near the edges of the square, in agreement with BCDI experiment results. To compare with the experimentally measured phase changes, the displacements shown along the dotted line in Figure 8.13b are extracted and superposed in Figure 8.12c (red dashed line). It can be seen that they have very similar decay behaviors. The simulated displacement indeed follows an exponential decay from the edge and the fitted decay length is 45 nm, which is reasonably consistent with the experiment results. The above results demonstrate the ability of BCDI to probe the local strain on the nanoscale, as well as the morphological subtleties in semiconductor devices. It also shows that the magnitude of the strain relaxation in submicron and nanoscale sSOI structures will be significant and should be taken into consideration in the design and

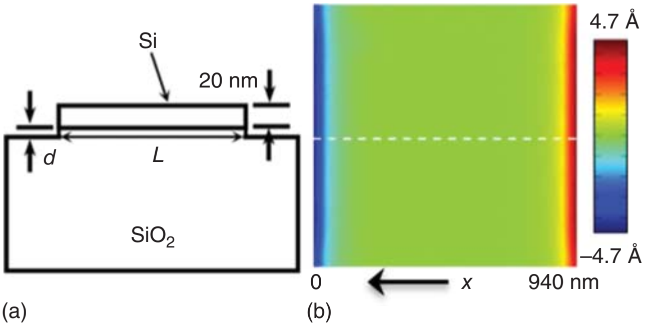

Figure 8.13 Schematic side view of the modeling system (a) and the simulated in-plane displacement in the x direction (b).

fabrication of sSOI-based devices. It is worth noting that the edge relaxation strain measured by BCDI is the local strain due to the patterning, while the initial tensile strain is global. The absolute strain of the patterned structure is the combination of the edge relaxation strain and the initial strain. As the initial biaxial tensile strain becomes relaxed, the band splitting and the resulting reduction in carrier average effective mass and intra-/inter-band scattering will not be as effective, and the carrier mobility enhancement will decay. It is also expected that the near oxide region becomes highly strained and near-surface region can be fully relaxed [137]. This nonuniform redistribution of strain on the nanoscale will impact the electrical and optical properties. Future Work is planned to perform *in situ* BCDI measurements while operating the sSOI device, to directly correlate the strain distribution with the electrical performance figure-of-merit of the device.

One expected concern in measuring micro- or nanoscaled samples using synchrotron source is radiation damage. In our previous work, we observed that the Si nanowires patterned on SOI substrate started showing signs of radiation-induced damage when the total dose exceeded 1×10^{10} Gy (J kg^{-1}) [80]. In the current experiment, we measured the diffraction by rotating the sample over a range of 0.6° with a step size of 0.01°, and a 25 s exposure time at each step. This corresponds to a total exposure time of ~25 min. The coherent flux of the beamline is approximately 10^9 photons s^{-1} over the focal spot with an area of 1.5 μm^2. One measurement would cause 1.5×10^{12} photon to be absorbed, amounting to a dose of 2.5×10^9 Gy (J kg^{-1}). Compared with our previous work, it can be seen that the dose in this experiment is well within the safety range. We repeated the measurement a couple of times immediately after the first one, and found that both the diffraction pattern and the reconstructions remained unchanged. It is also worth pointing out that the presence of already existing defects will be the vulnerable part of the structure. For samples from the same material but with different existing fault states (e.g., due to different process conditions), the properties associated with radiation damage will be different [138].

8.4.2.2 Strain Relaxation in Multiple sSOI Nanostructures

In a subsequent experiment, we attempted to measure strain effects in more complicated sSOI structures. sSOI wire arrays were fabricated using an sSOI substrate from similar wafers to those used for fabricating the above square sSOI structure, with the E-beam lithography and RIE etch-patterning process. The array consists of 11 parallel wires with a dimension of 100 nm × 1 μm and a 100 nm separation between them. The experiment geometry is the same as the one shown in Figure 8.10, with the long edges of the wires facing the incident beam. Figure 8.14a shows the diffraction pattern (central frame along the (−111) Bragg reflection) from the wire array. The sample was measured at the 34-ID-C beamline, but with a more efficient "Medipix" detector, capable of photon counting over a 256 × 256 sensor array. Because the diffraction pattern extended quite far in the vertical direction, the detector is not large enough to collect the full pattern in this direction. The cut-off of high frequency signals limited the reconstruction resolution as will see in the following discussion.

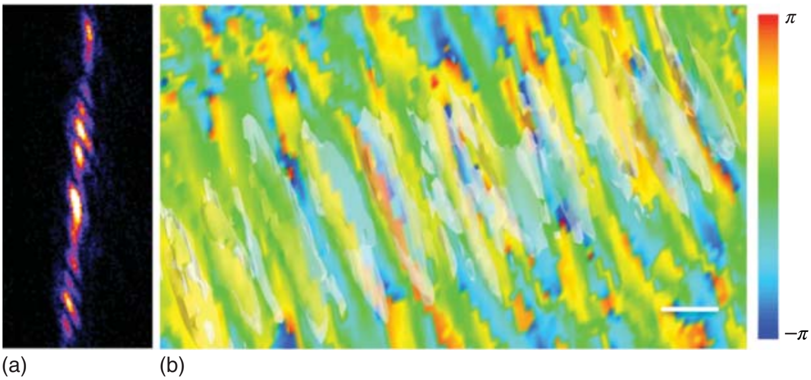

Figure 8.14 Diffraction pattern (central frame of the (−111) reflection) for an array of 11 sSOI wires (a); and the reconstructed phase map with the amplitude (translucent white) superimposed (b). scale bar = 300 nm.

Figure 8.14a appears to be quite a complicated pattern and the fringes are mostly along the vertical direction. This is due to the interference of the wires in the array. Figure 8.14b shows the reconstructed phase map, with the amplitude isosurface (shown in translucent white color) superimposed. There are 11 strips and each with a phase wrap along the wire horizontal edge direction. This is consistent with the strain relaxation behaviors due to the patterning process as seen in the square sSOI structure. However, the resolution achievable here was not high enough for resolving the relaxation inside each individual wire quantitatively. With improvement of beamline optics and detector techniques, higher quality data set might be obtained to allow further detailed analysis for strain relaxation properties in more complicated structures involved in industrial processes.

8.5 Conclusion

BCDI has undergone rapid development since its first demonstration about a decade ago for both the experimental method and the reconstruction algorithms. New applications in materials/nanoscience have been pursued. To date, most of the BCDI work has been conducted on third generation synchrotron radiation sources, and the best spatial resolution achieved is around 10–20 nm. The strain sensitivity, in the few pm range, has demonstrated great utility. With the advent of new coherent X-ray sources such as high harmonic generation and X-ray free-electron lasers, BCDI has the potential to be the method of choice for investigating sub-nanometer and atomic behavior in three dimensions for nanomaterials, providing unprecedented insights into the strain distribution in semiconductor devices and functional materials under extreme conditions, as well as many fundamental processes such as diffusion, phase transitions, catalysis, and imaging phonons (lattice dynamic) in nanocrystals. Its related research and applications will be even more exciting and rewarding in the coming decade.

Acknowledgements

Part of the work described in this article is supported by the European Research Council as an FP7 Advanced grant “Nanosculpture,” code 227711, and the work at MPI-Halle by the German Federal Ministry of Education and Research in the framework of the DECISIF project (Contract No. 13 N 9881).

References

1 Bartels, R.A., Paul, A., Green, H., Kapteyn, H.C., Murname, M.M., Backus, S., Christov, I.P., Liu, Y., Attwood, D., and Jacobsen, C. (2002) Generation of spatially coherent light at extreme ultraviolet wavelengths. *Science*, **297**, 376–378.

2 Takayama, Y., Tai, R.Z., Hatano, T., Miyhara, T., Okamoto, W., and Kagoshima, Y. (1998) Measurement of the coherence of synchrotron radiation. *J. Synchrotron Radiat.*, **5**, 456–458.

3 van der Veen, F. and Pfeiffer, F. (2004) Coherent X-ray scattering. *J. Phys. Condens. Matter*, **16**, 5003–5030.

4 Vlieg, E., de Vries, S.A., Alvarez, J., and Ferrer, S. (1997) Slits as adjustable pinholes for coherent X-ray scattering experiments. *J. Synchrotron Radiat.*, **4**, 210–213.

5 Bongaerts, J.H.H., David, C., Drakopoulos, M., Zwanenburg, M.J., Wegdam, G.H., Lackner, T., Keymeulen, H., and van der Veen, J.F. (2002) Preparation of a partially coherent focused X-ray beam within a planar X-ray waveguide. *J. Synchrotron Radiat.*, **9**, 383–393.

6 Kohn, V., Snigireva, I., and Snigirev, A. (2000) Direct measurement of transverse coherence length of hard X-rays from interference fringes. *Phys. Rev. Lett.*, **85**, 2745–2748.

7 Sandy, A.R., Lurio, L.B., Mochrie, S.G.J., Malik, A., Stephenson, G.B., Pelletier, J.F., and Sutton, M. (1999) Design and characterization of an undulator beamline optimized for small-angle coherent X-ray scattering at the Advanced Photon Source. *J. Synchrotron Radiat.*, **6**, 1174–1184.

8 Goodman, J.W. (1985) *Statistical Optics*, John Wiley & Sons, Inc., New York.

9 Giannini, C., Diaz, A., and Favre-Nicolin, V. (2010) Coherent diffraction imaging: basic concepts and applications, in *Diffraction at the Nanoscale Nanocrystals, Defective and Amorphous Materials* (eds A. Guagliardi and N. Masciocchi), Insubria University Press.

10 Gerchberg, R.W. and Saxton, W.O. (1972) A practical algorithm for the determination of phase from image and diffraction plane pictures. *Optik*, **35**, 237–246.

11 Miao, J., Sayre, D., and Chapman, H.N. (1998) Phase retrieval from the magnitude of the Fourier transforms of non-periodic objects. *J. Opt. Soc. Am. A*, **15**, 1662–1669.

12 Fienup, J.R. (1978) Reconstruction of an object form the modulus of its Fourier transform. *Opt. Lett.*, **3**, 27–29.

13 Fienup, J.R. (1982) Phase retrieval algorithms: a comparison. *Appl. Opt.*, **21**, 2758–2769.

14 Bates, R.H.T. (1982) Fourier phase problems are uniquely solvable in mute than one dimension. I: Underlying theory. *Optik*, **61**, 247–262.

15 Fienup, J.R. (1986) Phase retrieval using boundary conditions. *J. Opt. Soc. Am. A*, **3**, 284–288.

16 Bruck, Y.M. and Sodin, L.G. (1979) On the ambiguity of the image reconstruction problem. *Opt. Commun.*, **30**, 304–308.

17 Hayes, M.H. (1982) The reconstruction of a multidimensional sequence from the phase or magnitude of its Fourier transform. *IEEE Trans. Acoust. Speech Signal Process.*, **ASSP-30**, 140–154.

18 Fienup, J.R. (1987) Reconstruction of a complex-valued object from the modulus of its Fourier transform using a support constraint. *J. Opt. Soc. Am. A*, **4**, 118–123.

19 Fienup, J.R. and Wackerman, C.C. (1986) Phase-retrieval stagnation problems and solutions. *J. Opt. Soc. Am. A*, **3**, 1897–1907.

20 Williams, G.J., Pfeifer, M.A., Vartanyants, I.A., and Robinson, I.K. (2007) Effectiveness of iterative algorithms in recovering phase in the presence of noise. *Acta Crystallogr., Sect. A: Found. Crystallogr.*, **63**, 36–42.

21 Chen, C.C., Miao, J., Wang, C.L., and Lee, T.K. (2007) Application of optimization technique to noncrystalline X-ray diffraction microscopy: guided hybrid input–output method. *Phys. Rev. B*, **76**. doi: 10.1103/physrevb.76.064113

22 Elser, V. (2003) Phase retrieval by iterated projections. *J. Opt. Soc. Am. A*, **20**, 40–55.

23 Elser, V., Rankenburg, I., and Thibault, P. (2007) Searching with iterated maps. *Proc. Natl. Acad. Sci. U.S.A.*, **104**, 418–423.

24 Marchesini, S. (2007) Phase retrieval and saddle-point optimization. *J. Opt. Soc. Am. A*, **24**, 3289–3296.

25 Bauschke, H.H., Combettes, P.L., and Luke, D.R. (2003) Hybrid projection-reflection method for phase retrieval. *J. Opt. Soc. Am. A*, **20**, 1025–1034.

26 Luke, D.R. (2005) Relaxed averaged alternating reflections for diffraction imaging. *Inverse Prob.*, **21**, 37–49.

27 Oszlanyi, G. and Suto, A. (2008) The charge flipping algorithm. *Acta Crystallogr., Sect. A: Found. Crystallogr.*, **64**, 123–134.

28 Candes, E.J., Eldar, Y.C., Strohmer, T., and Voroninski, V. (2013) Phase retrieval via matrix completion. *SIAM J. Imag. Sci.*, **6**, 199–225.

29 Marchesini, S., He, H., Chapman, H., Hau-Riege, S., Noy, A., Howells, M., Weierstall, U., and Spence, J. (2003) X-ray image reconstruction from a diffraction pattern alone. *Phys. Rev. B*, **68**. doi: 10.1103/physrevb.68.140101

30 Miao, J.W., Charalambous, P., Kirz, J., and Sayre, D. (1999) Extending the methodology of X-ray crystallography to allow imaging of micrometre-sized non-crystalline specimens. *Nature*, **400**, 342–344.

31 Miao, J.W., Johnson, B., Anderson, E.H., Lai, B., and Hodgson, K.O. (2002) High resolution 3D X-ray diffraction microscopy. *Phys. Rev. Lett.*, **89**. doi: 10.1103/physrevlett.89.088303

32 Chapman, H.N., Barty, A., Marchesini, S., Noy, A., Hau-Riege, S.P. *et al.* (2006) High-resolution ab initio three-dimensional X-ray diffraction microscopy. *J. Opt. Soc. Am. A*, **23**, 1179.

33 Schroer, C.G., Boye, P., Feldkamp, J.M. *et al.* (2008) Coherent X-ray diffraction imaging with nanofocused illumination. *Phys. Rev. Lett.*, **101**. doi: 10.1103/physrevlett.101.090801

34 Takahashi, Y., Nishino, Y., Tsutsumi, R. *et al.* (2009) High-resolution diffraction microscopy using the plane-wave field of a nearly diffraction limited focused X-ray beam. *Phys. Rev. B*, **80**. doi: 10.1103/physrevb.80.054103

35 Barty, A., Marchesini, S., Chapman, H.N. *et al.* (2008) Three-dimensional coherent X-ray diffraction imaging of a ceramic nanofoam: determination of structural deformation mechanisms. *Phys. Rev. Lett.*, **101**. doi: 10.1103/physrevlett.101.055501

36 Jiang, H., Xu, R., Chen, C., Yang, W., Fan, J., Tao, X., Song, C., Kohmura, Y., Xiao, T., Wang, Y., Fei, Y., Ishikawa, T., Mao, W., and Miao, J. (2013) Three-dimensional coherent X-ray diffraction imaging of molten iron in mantle olivine at nanoscale resolution. *Phys. Rev. Lett.*, **110**. doi: 10.1103/physrevlett.110.205501

37 Williams, G.J., Quiney, H.M., Dhal, B.B., Tran, C.Q., Nugent, K.A., Peele, A.G., Paterson, D., and de Jonge, M.D. (2006) Fresnel coherent diffractive imaging. *Phys. Rev. Lett.*, **97**, 025506.

38 Quiney, H.M., Peele, A.G., Cai, Z., Paterson, D., and Nugent, K.A. (2006) Diffractive imaging of highly focused X-ray fields. *Nat. Phys.*, **2**, 101–104.

39 De Caro, L., Giannini, C., Pelliccia, D., Mocuta, C., Metzger, T.H., Guagliardi, A., Cedola, A., Burkeeva, I., and Lagomarsino, S. (2008) In-line holography and coherent diffractive imaging with X-ray waveguides. *Phys. Rev. B*, **77-R**. doi: 10.1103/physrevb.77.081408

40 Quiney, H.M., Nugent, K.A., and Peele, A.G. (2005) Iterative image reconstruction algorithms using wave-front intensity and phase variation. *Opt. Lett.*, **30**, 1638–1640.

41 Xiao, X. and Shen, Q. (2005) Wave propagation and phase retrieval in Fresnel diffraction by a distorted-object approach. *Phys. Rev. B*, **72**. doi: 10.1103/physrevb.72.033103

42 Nugent, K.A. (2010) Coherent methods in the X-ray science. *Adv. Phys.*, **59**, 1–99.

43 Abbey, B., Nugent, K.A., Williams, G.J., Clark, J.N., Peele, A.G., Pfeifer, M.A., de Jonge, M., and McNulty, I. (2008) Keyhole coherent diffractive imaging. *Nat. Phys.*, **4**, 394–398.

44 Abbey, B., Williams, G.J., Pfeifer, M.A., Clark, J.N., Putkunz, C.T., Torrance, A., McNulty, I., Levin, T.M., Peele, A.G., and Nugent, K.A. (2008) Quantitative coherent diffractive imaging of an integrated circuit at a spatial resolution of 20 nm. *Appl. Phys. Lett.*, **93**, 214101.

45 Peterson, I., Abbey, B., Putkunz, C.T., Vine, D.J., van Riessen, G.A., Cadenazzi, G.A., Balaur, E., Ryan, R., Quiney, H.M., McNulty, I., Peele, A.G., and Nugent, K.A. (2012) Nanoscale Fresnel coherent diffraction imaging tomography using ptychography. *Opt. Express*, **20**, 24678–24685.

46 Jones, M.W.M., van Riessen, G.A., Abbey, B. *et al.* (2013) Whole-cell phase contrast imaging at the nanoscale using Fresnel coherent diffractive imaging tomography. *Sci. Rep.*, **3**. doi: 10.1038/srep02288

47 Hoppe, W. (1969) Beugung im inhomogenen primarstrahlwellenfeld. I. Prinzip einer phasenmessung von elektronenbeungungsinterferenzen. *Acta Crystallogr., Sect. A: Found. Crystallogr.*, **25**, 495–501.

48 Faulkner, H.M.L. and Rodenburg, J.M. (2004) Movable aperture lensless transmission microscopy: a novel phase retrieval algorithm. *Phys. Rev. Lett.*, **93**. doi: 10.1103/physrevlett.93.023903

49 Rodenburg, J.M. and Faulkner, H.M.L. (2004) A phase retrieval algorithm for shifting illumination. *Appl. Phys. Lett.*, **85**, 4795–4797.

50 Thibault, P., Dierolf, M., Menzel, A., Bunk, O., David, C., and Pfeiffer, F. (2008) High-resolution scanning X-ray diffraction microscopy. *Science*, **321**, 379–382.

51 Schropp, A., Boye, P., Feldkamp, J.M. *et al.* (2010) Hard X-ray nanobeam characterization by coherent diffraction microscopy. *Appl. Phys. Lett.*, **96**, 091102.

52 de la Cuesta, F.B., Wenger, M.P.E., Bean, R.J., Horton, M.A., and Robinson, I.K. (2009) Coherent X-ray diffraction from collagenous soft tissues. *Proc. Natl. Acad. Sci. U.S.A.*, **106**, 15297–15301.

53 Robinson, I.K., Vartanyants, I.A., Williams, G.J., Pfeifer, M.A., and Pitney, J.A. (2001) Reconstruction of the shapes of gold nanocrystals using coherent X-ray diffraction. *Phys. Rev. Lett.*, **87**. doi: 10.1103/physrevlett.87.195505

54 Williams, G.J., Pfeifer, M.A., Vartanyants, I.A., and Robinson, I.K. (2003) Three-dimensional imaging of microstructure in Au nanocrystals. *Phys. Rev. Lett.*, **90**. doi: 10.1103/physrevlett.90.175501

55 Pfeifer, M.A., Williams, G.J., Vartanyants, I.A., Harder, R., and Robinson, I.K. (2006) Three-dimensional mapping of a deformation field inside a nanocrystal. *Nature*, **442**, 63–66.

56 Robinson, I. and Harder, R. (2009) Coherent X-ray diffraction imaging of strain at the nanoscale. *Nature Mater.*, **8**, 291–298.

57 Takagi, S. (1969) A dynamical theory of diffraction for a distorted crystal. *J. Phys. Soc. Jpn.*, **26**, 1239–1253.

58 Lemaitre, J. and Chaboche, J.L. (1994) *Mechanics of Solid Materials*, Cambridge University Press.

59 Newton, M.C., Leake, S.J., Harder, R., and Robinson, I.K. (2010) Three-dimensional imaging of strain in a single ZnO nanorod. *Nat. Mater.*, **9**, 120–124.

60 Clark, J.N., Huang, X., Harder, R., and Robinson, I.K. (2012) High-resolution three-dimensional partially coherent diffraction imaging. *Nat. Commun.*, **3**, 993.

61 Vartanyants, I. and Robinson, I. (2001) Partial coherence effects on the imaging of small crystals using coherent X-ray diffraction. *J. Phys.*, **13**, 10593–10611.

62 Leake, S.J., Newton, M.C., Harder, R., and Robinson, I.K. (2009) Longitudinal coherence function in X-ray imaging of crystals. *Opt. Express*, **17**, 15853–15859.

63 Williams, G.J., Quiney, H.M., Peele, A.G., and Nugent, K.A. (2007) Coherent diffractive imaging and partial coherence. *Phys. Rev. B*, **75**. doi: 10.1103/physrevb.75.104102

64 Huang, W.J., Zuo, J.M., Jiang, B., Kwon, K.W., and Shim, M. (2009) Sub-angstrom-resolution diffractive imaging of single nanocrystals. *Nat. Phys.*, **5**, 129–133.

65 Vartanyants, I.A. and Singer, A. (2010) Coherence properties of hard X-ray synchrotron sources and X-ray free-electron lasers. *New J. Phys.*, **12**, 035004.

66 Whitehead, L.W., Williams, G.H., Quiney, H.M. *et al.* (2009) Diffractive imaging using partially coherent X-rays. *Phys. Rev. Lett.*, **103**, 243902.

67 Clark, J.N. and Peele, A.G. (2011) Simultaneous sample and spatial coherence characterization using diffractive imaging. *Appl. Phys. Lett.*, **99**, 154103.

68 Chen, B., Dilanian, R.A., Teichmann, S. *et al.* (2009) Multiple wavelength diffractive imaging. *Phys. Rev. A*, **79**, 023809.

69 Abbey, B., Whitehead, L.W., Quiney, H.M. *et al.* (2011) Lensless imaging using broadband X-ray sources. *Nat. Photonics*, **5**, 420–424.

70 Harder, R., Liang, M., Sun, Y., Xia, Y., and Robinson, I.K. (2010) Imaging of complex density in silver nanocubes by coherent X-ray diffraction. *New J. Phys.*, **12**, 035019.

71 Watari, M., McKendry, R., Voegtli, M. *et al.* (2011) Differential stress induced by thiol adsorption on facetted nanocrystals. *Nat. Mater.*, **10**, 862–866.

72 Gulden, J., Yefanov, O.M., Mancuso, A.P. *et al.* (2012) Three-dimensional structure of a single colloidal crystal grain studied by coherent X-ray diffraction. *Opt. Express*, **20**, 4039–4049.

73 Robinson, I. (2013) Nanoparticle structure by coherent X-ray diffraction. *J. Phys. Soc. Jpn.*, **82**, 021012.

74 Beutier, G., Verdier, M., Parry, G. *et al.* (2013) Strain inhomogeneity in copper islands probed by coherent X-ray diffraction. *Thin Solid Films*, **530**, 120–124.

75 Harder, R. and Robinson, I. (2013) Coherent X-ray diffraction imaging of morphology and strain in nanomaterials. *J. Microsc.*, **65**, 1202–1207.

76 Favre-Nicolin, V., Mastropietro, F., Eymery, J. *et al.* (2010) Analysis of strain and stacking faults in single nanowires using Bragg coherent diffraction imaging. *New J. Phys.*, **12**, 035013.

77 Leake, S.J., Harder, R., and Robinson, I.K. (2011) Coherent diffractive imaging of solid state reactions in zinc oxide crystals. *New J. Phys.*, **13**, 113009.

78 Xiong, G., Huang, X., Leake, S., Newton, M.C., Harder, R., and Robinson, I.K. (2011) Coherent X-ray diffraction imaging of ZnO nanostructures under confined illumination. *New J. Phys.*, **13**, 033006.

79 Minkevich, A.A., Fohtung, E., Slobodskyy, T. *et al.* (2011) Strain field in (Ga, Mn)As/GaAs periodic wires revealed by coherent X-ray diffraction. *Europhys. Lett.*, **94**, 66001.

80 Shi, X., Xiong, G., Huang, X., Harder, R., and Robinson, I. (2012) Radiation-induced bending of silicon-on-insulator nanowires probed by coherent X-ray diffractive imaging. *New J. Phys.*, **14**, 063029.

81 Haag, S.T., Richard, M., Welzel, U. *et al.* (2013) Concentration and strain fields inside a Ag/Au core–shell nanowire studied by coherent X-ray diffraction. *Nano Lett.*, **13**, 1883–1889.

82 Cha, W., Song, S., Jeong, N.C., Harder, R., Yoon, K.B., Robinson, I.K., and Kim, H. (2010) Exploration of crystal strains using coherent X-ray diffraction. *New J. Phys.*, **12**, 035022.

83 Cha, W., Jeong, N., Song, S., Park, H., Pham, T., Harder, R., Lim, B., Xiong, G., Ahn, D., McNulty, I., Kim, J., Yoon, K., Robinson, I.K., and Kim, H. (2013) Core–shell strain structure of zeolite microcrystals. *Nat. Mater.*, **12**, 729–734.

84 Yang, W., Huang, X., Harder, R., Clark, J.N., Robinson, I.K., and Mao, H. (2013) Coherent diffraction imaging of nanoscale strain evolution in a single crystal under high pressure. *Nat. Commun.*, **4**, 1680.

85 Clark, J., Beitra, L., Xiong, G., Higginbotham, A., Fritz, D.M., Lemke, H.T., Zhu, D., Chollet, M., Williams, G.J., Messerschmidt, M., Abbey, B., Harder, R.J., Korsunsky, A.M., Wark, J.S., and Robinson, I.K. (2013) Ultrafast three-dimensional imaging of lattice dynamics in individual gold nanocrystals. *Science*, **341**, 56–59.

86 Tanaka, Y., Ito, K., Nakatani, T. *et al.* (2013) Time-resolved Bragg coherent X-ray diffraction revealing ultrafast lattice dynamics in nano-thickness crystal layer using X-ray free electron laser. *J. Ceram. Soc. Jpn.*, **121**, 283–286.

87 Xiong, G., Clark, J.N., Nicklin, C., Rawle, J., and Robinson, I.K. (2014) Atomic diffusion within individual gold nanocrystals. *Sci. Rep.*, **4**. doi: 10.1038/srep06765

88 Boutet, S. and Robinson, I.K. (2008) Coherent X-ray diffractive imaging of protein crystals. *J. Synchrotron Radiat.*, **15**, 576–583.

89 Aranda, M.A.G., Berenguer, F., Bean, R.J., Shi, X., Xiong, G., Collins, S.P., Nave, C., and Robinson, I.K. (2010) Coherent X-ray diffraction investigation of twinned microcrystals. *J. Synchrotron Radiat.*, **17**, 751–760.

90 Newton, M.C., Harder, R., Huang, X., Xiong, G., and Robinson, I.K. (2010) Phase retrieval of diffraction from highly strained crystals. *Phys. Rev. B*, **82**. doi: 10.1103/physrevb.82.165436

91 Vaxelaire, N., Proudhon, H., Labat, S., Kirchlechner, C., Keckes, J., Jacques, V., Ravy, S., Forest, S., and Thomas, O. (2010) Methodology for studying strain inhomogeneities in polycrystalline thin films during in situ thermal loading using coherent X-ray diffraction. *New J. Phys.*, **12**, 035018.

92 Shi, X., Xiong, G., Huang, X., Harder, R., and Robinson, I. (2010) Structural inhomogeneity in silicon-on-insulator probed with coherent X-ray diffraction. *Z. Kristallogr.*, **225**, 610–615.

93 Jacques, V.L.R., Ravy, S., Le Bolloc'h, D., Pinsolle, E., Sauvage-Simkin, M., and Livet, F. (2011) Bulk dislocation core dissociation probed by coherent X-ray in silicon. *Phys. Rev. Lett.*, **106**. doi: 10.1103/physrevlett.106.065502

94 Huang, X., Harder, R., Xiong, G., Shi, X., and Robinson, I. (2011) Propagation uniqueness in three-dimensional coherent diffractive imaging. *Phys. Rev. B*, **83**. doi: 10.1103/physrevb.83.224109

95 Chen, B., Zhang, F., Berenguer, F., Bean, R., Kewish, C., Vila-Comamala, J., Chu, Y., Rodenburg, J., and Robinson, I. (2011) Coherent X-ray diffraction imaging of paint pigment particles by scanning a phase plate modulator. *New J. Phys.*, **13**, 103022.

96 Huang, X., Harder, R., Leake, S., Clark, J., and Robinson, I. (2012) Three-dimensional Bragg coherent diffraction imaging of an extended ZnO crystal. *J. Appl. Crystallogr.*, **45**, 778–784.

97 Pinsolle, E., Kirova, N., Jacques, V.L.R., Sinchenko, A.A., and LeBolloc'h, D. (2012) Creep, flow, and phase slippage regimes: an extensive view of the sliding charge-density wave revealed by coherent X-ray diffraction. *Phys. Rev. Lett.*, **109**. doi: 10.1103/physrevlett.109.256402

98 Moore, G.E. (1965) Cramming more components onto integrated circuits. *Electronics*, **38**, 114–117.

99 International Technology Roadmap for Semiconductors (2012) http://public.itrs.net (accessed 20 September 2017).

100 Colinge, J.P. (1997) *Silicon-on-Insulator Technology: Materials to VLSI*, 2nd edn, Kluwer.

101 Celler, G.K. (1994) Silicon-on-insulator structures: fabrication, in *The Encyclopedia of Advanced Materials*, Pergamon, New York.

102 Pelloie, J.L. and Auberton-Herve, A. (2001) A new generation of IC process: low-power, high-performance SOI CMOS. *Solid State Technol.*, **44**, 63–66.

103 Vandooren, A., Jovanovic, D., Egley, S., Sadd, M., Nguyen, B.Y., White, B., Orlowski, M., and Mogab, J. (2002) Scaling assessment of fully-depleted SOI technology at the 30 nm gate length generation. Proceedings of the IEEE International SOI Conference Williamsburg, VA, IEEE, Piscataway, NJ, pp. 25–27.

104 Fossum, J.G., Trivedi, V.P., and Wu, K. (2002) Extremely scaled fully depleted SOI CMOS. Proceedings of the IEEE International SOI Conference Williamsburg, IEEE, Piscataway, NJ, pp. 135–136.

105 Celler, C.K. and Cristoloveanu, S. (2003) Frontiers of silicon-on-insulator. *J. Appl. Phys.*, **93**, 4955–4978.

106 Rudenko, T., Kilchytska, V., Colinge, J.P., Dessard, V., and Flandre, D. (2001) On the high-temperature subthreshold slope of thin-film SOI MOSFETs. *IEEE Electron Device Lett.*, **23**, 148–150.

107 Langdo, T.A., Lochtefeld, A., Currie, M.T. *et al.* (2002) Preparation of novel SiGe-free strained Si on insulator substrates. Proceedings of the IEEE International SOI Conference Williamsburg, IEEE, Piscataway, NJ, pp. 211–212.

108 Reiche, M., Moutanabbir, O., Himcinschi, C. *et al.* (2008) Strained silicon on wafer level by waferbonding: materials processing, strain measurements and strain relaxation. *ECS Trans.*, **16**, 311–320.

109 Sun, G., Sun, Y., Nishida, T., and Thompson, S.E. (2007) Hole mobility in silicon inversion layers: stress and surface orientation. *J. Appl. Phys.*, **102**, 084501.

110 Suthram, S., Ziegert, J.C., Nishida, T., and Thompson, S.E. (2007) Piezoresistance coefficients of (100) silicon nMOSFETs measured at low and high (~1.5 GPa) channel stress. *IEEE Electron Device Lett.*, **28**, 58–61.

111 Leong, M., Doris, B., Kedzierski, J., Rim, K., and Yang, M. (2004) Silicon device scaling to the sub-10-nm regime. *Science*, **306**, 2057–2060.

112 Rahman, A., Lundstrom, M.S., and Ghosh, A.W. (2005) Generalized effective-mass approach for n-type metal-oxide-semiconductor

field-effect-transistors on arbitrarily oriented wafers. *J. Appl. Phys.*, **97**, 053702.

113 Sun, Y., Thompson, S.E., and Nishida, T. (2007) Physics of strain effects in semiconductors and metal-oxide-semiconductor field-effect transistors. *J. Appl. Phys.*, **101**, 104503.

114 Lundstrom, M. (2000) *Fundamentals of Carrier Transport*, Cambridge University Press.

115 Shimizu, A., Hachimine, K., Ohki, N., Ohta, H., Koguchi, M., Nonaka, Y., Sato, H., and Ootsuka, F. (2001) Local mechanical-stress control (LMC): a new technique for CMOS-performance enhancement. International Electron Devices Meeting, pp. 433–436.

116 Gannavaram, S., Pesovic, N., and Ozturk, M.C. (2000) Low temperature recessed junction selective silicon-germanium source/drain technology for sub-70 nm CMOS. International Electron Devices Meeting, pp. 437–440.

117 Tarun, A., Hayazawa, N., Ishitobi, H., Kawata, S., Reiche, M., and Moutanabbir, O. (2011) Mapping the forbidden transverse-optical phonon in single strained silicon (100) nanowire. *Nano Lett.*, **11**, 4780–4788.

118 Moutanabbir, O., Reiche, M., Hahnel, A., Erfurth, W., Gosele, U., Motohashi, M., Tarun, A., Hayazawa, N., and Kawata, S. (2010) Nanoscale patterning induced strain redistribution in ultrathin strained Si layers on oxide. *Nanotechnology*, **21**, 134013.

119 Koester, S.J., Rim, K., Chu, J.O., Mooney, P.M., Ott, J.A., and Hargrove, M.A. (2001) Effect of thermal processing on strain relaxation and interdiffusion in Si/SiGe heterostructures studied using Raman spectroscopy. *Appl. Phys. Lett.*, **79**, 2148–2150.

120 Lei, R.Z., Tsai, W., Aberg, I., O'Reilly, T.B., Hoyt, J.L., Antoniadis, D.A., Smith, H.I., Paul, A.J., Green, M.L., Li, J., and Hull, R. (2005) Strain relaxation in patterned strained silicon directly on insulator structures. *Appl. Phys. Lett.*, **87**, 251926.

121 Himcinschi, C., Singh, R., Radu, I., Milenin, A.P., Erfurth, W., Reiche, M., Gösele, U., Christiansen, S.H., Muster, F., and Petzold, M. (2007) Strain relaxation in nanopatterned strained silicon round pillars. *Appl. Phys. Lett.*, **90**, 021902.

122 Jain, S.C., Maes, H.E., Pinardi, K., and De Wolf, I. (1996) Stresses and strains in lattice-mismatched stripes, quantum wires, quantum dots, and substrates in Si technology. *J. Appl. Phys.*, **79**, 8145–8165.

123 Moutanabbir, O., Reiche, M., Hahnel, A., Erfurth, W., Motohashi, M., Tarun, A., Hayazawa, N., and Kawata, S. (2010) UV-Raman imaging of the in-plane strain in single ultrathin strained silicon-on-insulator patterned structure. *Appl. Phys. Lett.*, **96**, 233105.

124 Tarun, A., Hayazawa, N., Balois, M.V., Kawata, S., Reiche, M., and Moutanabbir, O. (2013) Stress redistribution in individual ultrathin strained silicon nanowires: a high-resolution polarized Raman study. *New J. Phys.*, **15**, 053042.

125 Armigliato, A., Balboni, R., Carnevale, G.P., Pavia, G., Piccolo, D., Frabboni, S., Benedetti, A., and Cullis, A.G. (2003) Application of convergent beam electron diffraction to two-dimensional strain mapping in silicon devices. *Appl. Phys. Lett.*, **82**, 2172–2174.

126 Cooper, D., Be´ che´, A., Hartmann, J.-M., Carron, V., and Rouvie're, J.-L. (2010) Application of convergent beam electron diffraction to two-dimensional strain mapping in silicon devices. *Appl. Phys. Lett.*, **96**, 113508.

127 Hähnel, A., Reiche, M., Moutanabbir, O., Blimtritt, H., Geisler, H., Hoentschel, J., and Engelmann, H.J. (2012) Improving accuracy and precision of strain analysis by energy-filtered nanobeam electron diffraction. *Microsc. Microanal.*, **18**, 229–240.

128 Murray, C.E., Yan, H.F., Noyan, I.C., Cai, Z., and Lai, B. (2005) High resolution strain mapping in heteroepitaxial thin-film features. *J. Appl. Phys.*, **98**, 013504.

129 Murray, C.E., Polvino, S.M., Noyan, I.C., Cai, Z., Maser, J., and Holt, M. (2013) Probing strain at the nanoscale with X-ray diffraction in microelectronic materials induced by stressor elements. *Thin Solid Films*, **530**, 85–90.

130 Cohen, G.M., Mooney, P.M., Jones, E.C., Chan, K.K., Solomon, P.M., and Wong, H.S.P. (1999) Characterization of the silicon on insulator film in bonded wafers by high resolution X-ray diffraction. *Appl. Phys. Lett.*, **75**, 787–789.

131 Gailhanou, M., Loubens, A., Micha, J.S., Charlet, B., Minkevich, A.A., Fortunier, R., and Thomas, O. (2007) Strain field in silicon on insulator lines using high resolution X-ray diffraction. *Appl. Phys. Lett.*, **90**, 111914.

132 Baumbach, T. and Lübbert, D. (1999) Grazing incidence diffraction by laterally patterned semiconductor nanostructures. *J. Phys. D*, **32**, 726–740.

133 Godard, P., Carbone, G., Allain, M., Mastropietro, F., Chen, G., Capello, L., Diaz, A., Metzger, T.H., Stangl, J., and Chamard, V. (2011) Three-dimensional high-resolution quantitative microscopy of extended crystals. *Nat. Commun.*, **2**, 568.

134 Hruszkewycz, S.O., Holt, M.V., Murray, C.E., Bruley, J., Holt, J., Tripathi, A., Shpyrko, O.G., McNulty, I., Highland, M.J., and Fuoss, P.H. (2012) Quantitative nanoscale imaging of lattice distortions in epitaxial semiconductor heterostructures using nanofocused X-ray Bragg projection ptychography. *Nano Lett.*, **12**, 5148–5154.

135 Xiong, G., Moutanabbir, O., Huang, X., Paknejad, S.A., Shi, X., Harder, R., Reiche, M., and Robinson, I.K. (2011) Elastic relaxation in an ultrathin strained silicon-on-insulator structure. *Appl. Phys. Lett.*, **99**, 114103.

136 Hu, S.M. (1979) Film-edge-induced stress in substrates. *J. Appl. Phys.*, **50**, 4661–4666.

137 Moutanabbir, O., Reiche, M., Hahnel, A., Oehme, M., and Kasper, E. (2010) Multiwavelength micro-Raman analysis of strain in nanopatterned ultrathin strained silicon-on-insulator. *Appl. Phys. Lett.*, **97**, 053105.

138 Favre-Nicolin, V., Eymery, J., Koester, R., and Gentile, P. (2009) Coherent-diffraction imaging of single nanowires of diameter 95 nanometers. *Phys. Rev. B*, **79**. doi: 10.1103/physrevb.79.195401